Mon. Not. R. Astron. Soc. **000**, 000–000 (0000) Printed 28 August 1997 (MN LATEX style file v1.4)

Spectropolarimetric observations of active stars

J.-F. Donati[1], M. Semel[2], B.D. Carter[3], D.E. Rees[4] and A.C. Cameron[5]

[1] *Laboratoire d'Astrophysique, Observatoire Midi-Pyrénées, F–31400 Toulouse, France (*`donati@obs-mip.fr`*)*

[2] *DASoP, Observatoire de Paris-Meudon, F-92195 Meudon-Cedex, France (*`semel@obspm.fr`*)*

[3] *Faculty of Sciences, The Univ. of Southern Queensland, Toowoomba 4350, Australia (*`carterb@usq.edu.au`*)*

[4] *CSIRO Division of Radiophysics, PO Box 76, Epping, NSW 2121, Australia (*`drees@rp.csiro.au`*)*

[5] *School of Physics and Astronomy, Univ. of St Andrews, St Andrews, Scotland KY16 9SS (*`acc4@st-andrews.ac.uk`*)*

Received December 1996; accepted 1997

ABSTRACT

This paper reports the results of 5 yr (5 runs, 23 nights) of spectropolarimetric observations of active stars with the UCL Echelle Spectrograph of the Anglo-Australian Telescope. Two hundred and twenty five circularly (and four linearly) polarised spectra were recorded on 28 objects (21 active stars and 7 calibration standards) using the new technique of Zeeman-Doppler imaging.

To extract polarisation échelle spectra from raw frames, we developed a new dedicated automatic software package (called ESpRIT and utilizing optimal extraction techniques) whose detailed description is given in the paper. For each recorded spectrum, we extract "mean" polarised and unpolarised profiles using "Least-Squares Deconvolution", a technique similar to cross-correlation which can enhance enormously the sensitivity of Zeeman-Doppler imaging, by up to 7.5 mag in flux with respect to a single average line analysis or by 4.5 mag compared to the older technique of Donati et al. (1992a) in the particular case of a K1 star.

Magnetic field is detected unambiguously on 14 objects, namely the weak-line T Tauri star V410 Tau, the pre-main sequence binary HD 155555, the ZAMS stars AB Dor and LQ Hya, the dwarf flare star CC Eri, the RS CVn systems HR 1099, EI Eri, TY Pyx, CF Tuc, SZ Psc, II Peg, IM Peg and IL Hya, and the FK Com star YY Men. Marginal field detections are also obtained for the weak-line T Tauri star HD 283572 and the Herbig Ae star HD 104237. Except on HR 1099 and II Peg, our results represent the first *direct* field detections ever reported on these objects, and in particular the first *direct* field detection on as young a star as V410 Tau. Most of the magnetic signatures we detect on cool stars show several sign reversals throughout the line profile, witnessing that the parent field structure is rather complex and must feature (as expected) many small-scale magnetic regions of different polarities. For all stars on which Zeeman detections are recorded with sufficient accuracy (namely LQ Hya, CC Eri, HR 1099, EI Eri, II Peg, IL Hya and YY Men), differential Least-Squares Deconvolution from both the blue and red parts of the spectral domain indicates that the magnetic regions we detect are mostly 500 to 1,000 K cooler than, sometimes at the same temperature as, but never warmer than the surrounding photosphere.

Serendipitous results include the first detection (i) of small amplitude radial velocity variations (1.3 $\mathrm{km\,s^{-1}}$ peak to peak) of the Herbig Ae star HD 104237 with small enough a period (37.5 ± 1 min) that they must be due to stellar pulsations; and (ii) of the solar-like secondary component of the RS CVn system IL Hya.

Key words: Line: profiles – Polarisation – Stars: activity – Stars: atmospheres – Stars: late-type – Stars: magnetic fields

1 INTRODUCTION

Activity phenomena in most cool stars are found to be similar to those observed on the Sun, but with different strengths and variability timescales. This is why they are also attributed to dynamo mechanisms operating in their convective envelopes. Most of what we know today about dynamo action in stellar atmospheres comes from observations of the Sun, whose proximity allows very detailed and well documented analyses of the associated activity phenomena. However, despite several decades of efforts, theoreticians have not yet arrived at an adequate, self-consistent MHD model of the solar convective zone that reproduces quantitatively all relevant observations at the same time. Even if much poorer in terms of spatial resolution, stellar observations represent a very rich potential source of information as they can tell us how dynamo processes depend on fundamental parameters such as mass, age, photospheric temperature and rotational velocity. In particular, it would be very valuable to access, for a large sample of objects, information on their magnetic topologies, as well as the evolution of the field structure throughout a full activity cycle.

Due to the complexity of solar-type magnetic configurations (featuring many bipolar groups over the stellar surface), attempts to detect such fields on other stars via conventional methods (measuring line shifts between left and right circular polarisation spectra) have yielded inconclusive results, being sensitive only to the line-of-sight component of the disk-integrated vector field (Brown & Landstreet 1981; Borra et al. 1984). Most magnetic field measurements available to date have been obtained with the so-called "Robinson technique", measuring differential Zeeman broadening between magnetically sensitive and insensitive spectral lines (Robinson 1980). However, this technique suffers from large systematic errors (Saar & Solanki 1992; Rüedi et al. 1997) and cannot be applied to the most active objects (the rapid rotators for which Zeeman broadening becomes undetectable). Although infrared observations can partly solve the first point as demonstrated recently by Valenti et al. (1995), the problem remains that the method is not informative enough about the actual magnetic field *structure* for any accurate testing of dynamo predictions.

A new alternative was proposed a few years ago, based on the so-called Zeeman enhancement of spectral lines in the presence of a magnetic field (Basri et al. 1992; Basri & Marcy 1994). Although it can in principle be applied to moderate rotators, it is still marginally conclusive and does not offer any improvement over the previous options for yielding structural information on the field topology. In an attempt to generalise this technique, Saar et al. (1992, 1994) proposed to link it to a surface imaging package (Doppler imaging) in order to locate at the surface of the star (through rotational modulation of magnetically sensitive line profiles) those regions responsible for the observed Zeeman enhancement of spectral lines. However, given the complex sensitivity of unpolarised profiles to vector properties of the magnetic field, one still needs to assume some arbitrary field orientation (radial in Saar et al.'s work) for the reconstruction. Moreover, the small overall strength of the Zeeman enhancement signal and its close resemblance to signatures from temperature inhomogeneities make results from this (yet untested) technique somewhat ambiguous and unreliable.

The new method proposed by Semel (1989) called Zeeman-Doppler imaging (ZDI) consists of looking for circular polarisation profiles in lines of rapidly rotating active stars. For these objects, the Doppler effect isolates in wavelength, in disc-integrated profiles, contributions from stellar regions with different instantaneous radial velocities; close bipolar groups should thus no longer cancel their mutual effect in circular polarisation profiles (as in conventional polarisation techniques) as long as opposite polarities are associated with different radial velocities. Moreover, it is far more reliable than all previous methods to date, circular polarisation in line profiles being unambiguously related to magnetic fields. This new method proved quite successful, allowing the first direct Zeeman detections in a number of active stars (Donati et al. 1990, 1992a). When linked to a surface imaging package (Brown et al. 1991; Donati & Brown 1997), this technique can even produce detailed maps of the photospheric vector field (Donati et al. 1992b; Donati & Cameron 1997).

The main problem with this technique is still the overall very small size of the Zeeman signatures, typically 0.1% of the unpolarised continuum (Donati et al. 1992a). When using no more than a few spectral lines together, ZDI is thus limited to the few very bright active stars on which extremely high quality spectra can be recorded in the maximum integration time one can afford given the high rotation rate (typically one percent of the rotation period). In this new paper, we report results from new ZDI observations at the Anglo-Australian Telescope (AAT) with the UCL Echelle Spectrograph (UCLES). Subsequent efforts in developing a dedicated tool for accurate and rigorous extraction of such échelle spectra is described. We also demonstrate that the simultaneous use of numerous spectral lines yields drastic sensitivity improvements of up to 7.5 mag in flux (in the particular case of a K1 star), thus offering a possible solution for the above-mentioned problem. Zeeman signatures are unambiguously measured in 14 objects (and marginally in two others), including pre-main sequence cool and hot stars, ZAMS stars, main sequence flare stars and evolved RS CVn and FK Com objects. We finally discuss the potential implication of this new ZDI upgrade for future studies of stellar magnetic activity.

2 OBSERVATIONS

Five AAT/UCLES observing runs (23 nights) have been allocated in the last five years to this project. The instrumental setup is inspired by that used at the Canada-France-Hawaii Telescope (CFHT) in Sep. 1990 and Jan. 1991 (Donati et al. 1992a, 1992b; Semel et al. 1993). At the f/8 Cassegrain focus, we mount a visitor polarimeter built in Meudon and consisting of an aberration-free beamsplitter (Semel 1987) coupled to a commercial "achromatic" quarter-wave plate (whose retardance is accurate to within 3% in a 400 to 700 nm domain). The plate is oriented with respect to the beamsplitter to achieve a circular polarisation analysis of the stellar light. Attendant optics convert the input f/8 Cassegrain beam into a much slower one (on which the polarimetric analysis is performed) then back to a fast beam prior to injection into the double optical fibre (one fibre for each circular polarisation state) used to convey the light down to UCLES. The diameter of the fibre core projects to about 1.8″ on the sky. Note that the quarter-wave plate can be rotated by 90° back and forth (its optical axes switching from –45° to +45° with respect to those of the beamsplitter) so that both beams can be exchanged throughout the whole instrumentation.

Linear polarisation (Stokes Q and U) spectra can also be obtained with this setup, by aligning the optical axes of the quarter-wave plate with those of the beamsplitter and

Table 1. Setup characteristics. For each AAT run, the fibre core diameter d, the input and output f ratio ($f_{\rm i}$ and $f_{\rm o}$ respectively) used for the fibre, the magnification factor γ of the slicer attendant optics, the number of slices $n_{\rm s}$, the image size at the entrance of the spectrograph and at detector level ($s_{\rm i}$ and s_0 respectively), the spectrograph grating and detector configuration (79 and 31 for the 79 and 31.6 l/mm gratings respectively, Thx and Tek for the 1024×1024 pxl Thomson and Tektronix CCD detectors respectively), the first/last order numbers $n_{\rm o}$, the initial/final wavelengths λ and total wavelength coverage s_λ, the peak S/N per 3 km s^{-1} spectral bin reached on the K1IV star HR 1099 ($m_{\rm V}=5.8$) in a 20 min exposure, and the resolving power R, are listed in Cols. 2 to 14. The second entry for 1993 Dec. corresponds to a bluer setup used in the second half of the last night.

Run	d (μm)	$f_{\rm i}$	$f_{\rm o}$	γ	$n_{\rm s}$	$s_{\rm i}$ (mm^2)	$s_{\rm o}$ (pxl^2)	UCLES	$n_{\rm o}$	λ (nm)	s_λ (nm)	S/N (pxl^{-1})	R
1991 Aug.	150	4.5	3.1	11.6	3	0.60×10.5	2.4×64	79+Thx	34/46	488/665	62	550	57,000
1991 Dec.	100	3.0	2.8	12.9	4	0.34×10.5	1.4×64	79+Thx	33/46	490/686	67	520	75,000*
1992 Dec.	100	3.0	3.0	12.0	4	0.31×9.8	1.0×46	79+Tek	33/48	467/686	96	1,060	75,000*
1993 Dec.	100	3.0	3.0	12.0	4	0.31×9.8	1.0×46	79+Tek	32/48	467/708	105	1,130	75,000*
									36/50	448/628	85		
1995 Dec.	100	3.0	3.0	12.0	2	0.62×3.8†	2.0×18	31+Tek	81/123	460/706	235	750	55,000

$^\star R$ was apparently limited by internal aberrations and/or pixel crosstalk in the CCD
†A dekker was used to limit the length of the spectrograph slit and avoid order overlap

rotating the Cassegrain bonnette back and forth at azimuths 0° and 90° (for Stokes Q) and azimuths 45° and 135° (for Stokes U) with respect to the North–South direction. In the present study, such spectra are mainly used for calibration purposes (see Sect. 5.1.2).

A Bowen-Walraven image slicer with attendant optics is used at the entrance of the spectrograph to maximise slit throughput whatever slit width is selected. Attendant optics (see Semel et al. 1993 for details) include one short focal length doublet at the fibre output to slow down the beam to about f/80 (at which the slicing operation is performed), one long focal length doublet placed just before the slicer and acting as a field lens (i.e. projecting the pupil onto the spectrograph grating), and two doublets mounted before the spectrograph slit (at infinite conjugate ratio) whose respective focal lengths are tuned to obtain the requested overall magnification factor (about 12 in the present experiment) and to feed UCLES with a nominal f/36 beam. The effect of the slicer itself is, crudely speaking, to chop each circular image of the fibre end and align the resulting slices on top of each other. Increasing the number of slices results in a proportional increase/decrease in the height/width of the sliced image. The overall optical design is very flexible and allows to change the slicing configuration in a matter of minutes.

As one can see from Table 1 (listing for each run the quantitative characteristics of the optical design), the instrument has undergone considerable evolution between 1991 and 1995. In particular, the overall efficiency (defined by the peak S/N times the total wavelength coverage) has been multiplied by more than 5 between the first and last observing run.

Note that our non conventional fibre-feed disables the access to all usual UCLES calibration facilities. Flat-fielding and arc calibration are carried out using a halogen lamp and a thorium-argon hollow cathode mounted on wooden sticks and inserted manually into the beam by an observer in the Cassegrain cage. Despite initial concerns that variable positioning of the lamps might lead to problems with uneven illumination of the grating we verified that the arc-line positions are reproducible within 0.01 pxl on short timescales and 0.1 pxl throughout the night.

3 PROCESSING ÉCHELLE SPECTRA

Due to the special polarimetric setup of UCLES, the collected frames have a very peculiar format. In particular:

- Each order includes two separate spectra (one for each polarisation state) which need to be extracted either together (if one is not interested in the polarimetric information) or separately (otherwise). Moreover, the frames can feature a very complex order section profile whenever a Bowen-Walraven slicer is used (as is the case for our data).
- Since an order can be up to 65 pxl wide, the slit tilt with respect to CCD lines (due to the fact that the cross-dispersing prisms in UCLES are located ahead of the grating) produces a significant spectrum shift (up to 4 pxl in the dispersion direction) from one side of an order to the other.
- The Bowen-Walraven slicer generates distortion in the slit *shape*, whose total amplitude can reach up to 1 pxl (in the 2 slice configuration). Note as well that using a dekker (as in 1995 Dec.) results in slit *shape* asymmetries between both beams.

All these peculiarities present severe problems to most conventional reduction packages. For instance, the very complex order section profile makes the order localising task (usually limited to a simple Gaussian fit) much more complicated than usual. Considerably more problematic is the slit distortion and tilt with respect to CCD lines which, if neglected in the way that most existing extraction packages do, can limit drastically the final spectrum quality. A first consequence of this approximation is of course a dramatic loss in spectral resolution. Moreover, one must also realise that existing optimal extraction routines (assuming that wavelength is constant along either CCD lines or columns) should perform very poorly, especially in the case of sharp-lined stars. Even more crucial as far as polarisation is concerned, ignoring slit distortion and tilt should induce significant wavelength shifts between the two orthogonally polarised spectra within each order and thus generate spurious second-order polarisation signatures (see Sect. 5.1.1).

Rather than modifying existing routines, we decided to build a new software package from scratch that we called ESpRIT (for Echelle Spectra Reduction: an Interactive Tool). It performs optimal and rigorous extraction of échelle spectra, even in the case of highly distorted orders with tilted and wiggling slit profiles. It has also been designed for real time processing, and therefore tries to keep interactions with the observer to a minimum. In particular, all ancillary tasks (such as wavelength calibration) have been automated as much as possible. Although in a quite advanced stage already, ESpRIT is still under development, some points being subject to potential improvements in the future. We describe the actual version in the following paragraphs for the reader to get an idea on how our AAT data were processed, while the final version of the code will be presented separately in a forthcoming paper.

Input frames are assumed to be in FITS format while output spectra are recorded in ASCII (to ensure wider compatibility and easier manipulation). Byte swapping, plots and processing information are all optional and can be either enabled or disabled by simply invoking flags in the initial programme calls. The same version of the code has been successfully used to process data from various telescope/spectrograph combinations, which demonstrates its robustness and flexibility. Working under Unix, this new package is written in C in a very modular form (about 6,000 lines altogether) and should thus be very portable (testing has been completed successfully on Convex, Dec Alpha, Dec 5000, Sparc 10 and HP workstations so far).

Going from raw frames to échelle spectra takes several successive steps. The first one involves solving for all geometrical elements of the raw échelle frame (location and shape of orders, direction and shape of slit in each order), while the second one performs the wavelength calibration. Both are independent from one another, save all useful results in a disk file (for future access) and need only to be run once for each given spectrograph configuration. In the final step, the extraction of the intensity/polarisation spectrum is achieved through a generalised optimal extraction scheme. Each of these steps is detailed in the following paragraphs.

3.1 Geometrical elements of raw échelle frames

In this first step, the user provides three frames corresponding respectively to a flat field, an arc and a bias exposure. After trimming and mirroring operations on all images (to get rid of possible overscan rows and to come back to a standard situation with orders running vertically and wavelength increasing along orders with pixel number), the code subtracts a quadratic 2D fit to the bias image from both flat field and arc frames. From a user-provided estimate of the central location and width of the first order (used to derive a reference horizontal order section profile), the code locates and traces each order (in the flat field frame) by means of cross correlations with this reference order section profile. A 2D cubic fit to these measurements (the first dimension fitting the trace of each order, the other the variation of this trace from one order to the next) yields simultaneously the final equations for the location of all orders on the CCD.

From now on, this first set of equations is used to compute what we call the "central axis" (fractional row number of the order centre as a function of line number) of each order, as well as to determine their own domain on the CCD (spanning from mid-distance to the previous order to mid-distance to the next one). Within a given order, spectra of the arc frame *along the central axis* (one for each row) are then cross-correlated together to trace the shape of the arc lines perpendicularly to the dispersion. A linear or quadratic 2D fit to these measurements provides a second set of equations describing the slit *direction* (vertical pixel shift as a function of distance from central axis of the order) in all orders. Finally, the deviations from this mean polynomial slit direction (function of distance from central axis of order) are averaged over all orders, yielding an estimate of the mean slit *shape* (that we store as a double series of points).

Both sets of polynomial coefficients and the mean slit shape are recorded on disk for future reference. In particular, this information will be accessed prior to the spectrum extraction (see Sect. 3.4) to set up a new coordinate system within each order. After setting up an index array to access all CCD pixels by increasing or decreasing order number, we compute the curvilinear coordinates of each pixel in a "local order frame" that we store in two additional arrays (using the above mentioned index system); the first coordinate refers to the horizontal distance from the central axis of the order, while the second one notes the fractional line number of the pixel projection *along the slit profile* onto the central axis. These two arrays are especially useful to speed up the overall process as most extraction operations implicitly refer to this indexed curvilinear coordinate system.

Finally, we also store on disk the thorium spectrum extracted from the calibration frame, once each order is collapsed along slit direction and shape (see Sect. 3.3 for details) with a pixel sampling referred to the central axis.

3.2 Wavelength calibration

User input is minimum in this phase, being restricted to order numbers and rough estimates for the initial wavelength and pixel size of any given order within the spectrum. Using the uncalibrated arc spectrum (produced in the first step), the code attempts to calibrate the first selected order. Starting from an approximate linear dispersion equation provided by the user, the code tries to locate all lines that should be present in this portion of the spectrum according to a calibration line list and derives a more accurate quadratic dispersion polynomial. Note that only "unblended" calibration lines are used in this process, line pairs with separation smaller than two resolution elements being discarded a priori. We finally select the best result (minimising the misfit between measured and tabulated line wavelengths) among all attempts corresponding to various offset versions of the initial linear dispersion relation guess.

Once a reasonable (though still preliminary) dispersion relation is obtained for the first selected order, all other orders are calibrated successively following the same scheme, except that the initial dispersion relation guess is now a scaled version of that derived for the first calibrated order (the scaling factor being the ratio of order numbers). These preliminary calibrations are mainly intended to yield a proper *identification* of calibration lines, rather than an accurate dispersion relation. Since systematic errors can still arise in individual orders when too many lines are wrongly identified and/or when only very few lines are available within a given order, the final dispersion relation is obtained in a second pass by fitting a 2D polynomial to the pixel positions and corresponding wavelengths of *all* selected arc lines simultaneously (one dimension fitting the dispersion relation of each order, the second its variation from one order to the next). This way, every single arc line throughout the spectrum contributes to the calibration of each order, which all end up being homogeneously well calibrated.

Up to 43 orders are calibrated simultaneously in our AAT data (95 Dec. data set) and the code has proved to work successfully with 68 orders in other cases. Note that the 2D polynomial used for this calibration is actually the product of two 1D polynomials, a cubic one (in the direction that fits the dispersion relation of each order) and one of twelfth degree (for adjusting the variation of the dispersion relation from one order to the next). An automatic and iterative rejection process is also implemented for lines departing too strongly from their predicted position (i.e. whose identification is thus suspected to be wrong). This scheme is found to be very efficient, with mean rms calibration accuracies of better than 0.3 pm (i.e. 3 mÅ) in the case of our AAT spectra. The fitted wavelengths of arc lines observed twice in adjacent orders are also checked automatically and are found to agree within typically 0.05 pxl rms.

The final calibration polynomials (referring to the central axis) of each order are recorded on disk for future reference.

3.3 Optimal extraction of intensity spectra

Once these two steps are completed, extraction of stellar spectra can begin. ESpRIT requests the observer to provide three frames (corresponding respectively to one stellar, one flat field and one bias exposure) augmented by both data files produced in the steps described above (containing all information about trimming and mirroring operations, order shape, slit direction and shape, wavelength calibration). The last piece of information to provide is the characteristics of the CCD (gain and readout noise) for the code to set up a proper error array taking into account the exposure level in each individual pixel.

Once all frames are bias subtracted (see Sect. 3.1 for details), we set up the indexed curvilinear coordinate system described in Sect. 3.1 and to be used in most operations listed below. We then correct for pixel to pixel sensitivity differences by dividing each individual pixel in the stellar frame by its equivalent in the flat field image. As flat field and stellar frames happen to have the same horizontal order section profiles (as is often the case in fibre-fed instruments), it is necessary to "flatten down" each order of the flat field frame *prior to the pixel to pixel division*; keeping unaffected the *relative* exposure level between pixels throughout each line of each order in the stellar image is indeed important, as it conditions strongly the optimal extraction scheme. This flattening operation (still preliminary in the present version of the code) is achieved by dividing the original flat field frame by a model one obtained by propagating along the central axis of each order a *mean* horizontal section profile (measured on the central lines of the original flat field image). More sophisticated schemes (taking into account in particular possible variations of the horizontal section profile of an order along its central axis) are still under study. Relative flat field fluxes in each order are used later on (after interorder background removal) as a normalisation for the corresponding stellar fluxes.

To estimate interorder background, we look (in each line of the stellar image) for a minimum level in a narrow transition region between orders. We then subtract from the stellar frame a 2D polynomial fit through all these points. Once again, this 2D polynomial is actually the product of two 1D polynomials, a parabola fitting the interorder background and a sixth order polynomial adjusting its variation from one order to the next.

Complex horizontal order sections (like those obtained when using Bowen-Walraven slicers) in addition to moderate to large order tilts make the original optimal extraction scheme devised by Horne (1986) unusable. The trivial solution consisting in straightening the frames prior to invoke optimal extraction is not viable as it implies *resampling* noisy data; not only would the original noise statistics be ruined in this process but the data themselves can be corrupted, especially when sharp row-to-row flux gradients are present (see Allington-Smith 1989; Marsh 1989; Mukai 1990) as it is the case in our AAT data. Interpolating a model *onto the data* (rather than the opposite) is a much more preferable and rigorous approach. The solution we implemented here is that of Marsh (1989), except that we generalised it to account for possible tilts in the slit direction with respect to CCD lines.

To begin with, we derive a preliminary spectrum by collapsing the orders along the slit direction and shape and deconvolving it from the additional broadening induced by all linear interpolations involved. Note that we exclude from this process all pixels deviating too much from the average intensity over the order (strong cosmic ray hits). If one is interested in no more than a straightforwardly collapsed version of the spectrum to be recovered (e.g. thorium-argon lamp spectrum), we usually stop the process here. When full optimal extraction is required, we then construct a fake image by propagating this preliminary collapsed spectrum along the slit direction throughout each order, and by which we divide the actual stellar frame. In a second step, we apply Marsh's scheme to obtain the polynomial fits giving, in each order, the fractional fluxes as a function of distance from central axis. We finally try to obtain a new (and hopefully more accurate) spectrum by looking for a function whose interpolation onto the CCD pixels of each order (according to the geometrical elements derived in Sect. 3.1) multiplied by the polynomial fits to the fractional fluxes gives the original stellar frame. This last step is a standard linear inverse problem whose least squares solution is easy to obtain (tridiagonal matrix inversion in the case of linear interpolation). Both steps (fit to fractional fluxes and tridiagonal matrix inversion) involve an automatic and iterative cosmic ray rejection scheme. Note that the tridiagonal matrix to be inverted is actually nothing else than the problem *autocorrelation* matrix, from which accurate error bars can be obtained for each individual spectral pixel (e.g. Press et al. 1992).

In principle, this process can be repeated several times, with the output spectrum of a given iteration being used as the input guess in the following iteration. However, as no improvement in spectrum quality is observed in the following iterations, we usually stick to a single pass scheme to increase computing speed as much as possible. Such a generalisation of optimal extraction to échelle frames with tilted slit profiles is found to be just as rigorous and efficient as all previous versions as far as cosmic ray rejection, S/N optimisation and spectrophotometric accuracy are concerned, but produces in addition output spectra with no loss of spectral resolution. With this scheme, the output spectrum ends up automatically with a pixel sampling that refers to the central axis of each order and can thus be easily wavelength calibrated with the dispersion polynomials obtained in Sect. 3.2.

Automatic continuum normalisation is also implemented. When properly normalised and wavelength calibrated to flat field flux, the output of optimal extraction is a roughly continuous spectrum over the whole domain. In a first step, the code identifies continuum points throughout the entire spectrum and fits them globally by a high degree 1D polynomial. Then, any remaining systematic trends in the continuum shape from one order to the next are removed with the help of a new low degree 2D polynomial fit (one direction for the continuum shape in each order, the other for any weak variation in continuum shape among orders). Finally, the wavelength calibration is automatically corrected to refer to the heliocentric frame if all necessary information about the exposure and observatory can be found in the FITS file headers, or in the local Earth frame otherwise.

Sky contribution is neglected, most objects observed to date being brighter than $10^{\rm th}$ magnitude.

3.4 Optimal extraction of polarisation spectra

Optimal extraction of polarised spectra is very similar in principle to conventional extraction and differs mainly by the overall amount of processing involved. A polarisation observation consists of a sequence of four subexposures, each of them featuring two interleaving spectra corresponding to both orthogonal states of polarisation. The four subexposures are associated to two different azimuths of the retarding plate or Cassegrain bonnette (position 1, 2, 2 and 1 successively), each rotation amounting to no more than a beam switch throughout the whole instrumentation (see Sect. 2).

Each frame is processed according to the overall scheme of Sect. 3.3, both polarised states being optimally extracted independently. Note in particular that both orthogonally polarised spectra are obtained with the same wavelength sampling, making all subsequent differential operations between these spectra (see below) much easier. Once all four frames (i.e. eight spectra) are processed, the mean intensity spectrum I is derived by simply adding them up together while the polarisation rate P/I is given by:

$$\frac{P}{I} = \frac{R-1}{R+1} \tag{1}$$

where

$$R^4 = \frac{i_{1,\perp}/i_{1,\parallel}}{i_{2,\perp}/i_{2,\parallel}} \frac{i_{4,\perp}/i_{4,\parallel}}{i_{3,\perp}/i_{3,\parallel}} \tag{2}$$

$i_{k,\perp}$ and $i_{k,\parallel}$ noting respectively the two spectra obtained in subexposure k (see Tinbergen & Rutten 1992; Semel et al. 1993). In particular, one can first notice that polarisation is obtained by coherently dividing (rather than differentiating) spectra with orthogonal polarisation states (1/2 and 4/3). This method is very convenient to eliminate (to first order) all systematic errors and possible sources of spurious signals (stellar rotation and variability, Earth rotation, drifts in the spectrograph, inhomogeneities in CCD pixel sensitivities...) that may result from the fact that both polarisation states are not (and cannot be) recorded at the same time, on the same CCD pixels and through the same instrument channel (see Semel et al. 1993). Note that flat-fielding operations (see Sect. 3.3) are conserved although not strictly required in this particular case (pixel to pixel sensitivity variations being automatically removed through spectrum ratioing), in order to help optimal extraction behave correctly.

A "null polarisation" spectrum (called N/I in the following) can also be obtained by pair processing subexposures corresponding to identical azimuths of the retarding plate or Cassegrain bonnette (1/4 and 2/3 instead of 1/2 and 4/3), i.e. by replacing R in Eq. 1 by:

$$R^4 = \frac{i_{1,\perp}/i_{1,\parallel}}{i_{4,\perp}/i_{4,\parallel}} \frac{i_{2,\perp}/i_{2,\parallel}}{i_{3,\perp}/i_{3,\parallel}} \tag{3}$$

This quantity is particularly interesting to check still further that any potential signature in the polarisation profile is indeed real. Note that, if smaller exposure sequences (pairs of subexposures corresponding respectively to retarder azimuthal positions 1 and 2) can still be used to derive a polarisation rate (by replacing R in Eq. 1 by:

$$R^2 = \frac{i_{1,\perp}/i_{1,\parallel}}{i_{2,\perp}/i_{2,\parallel}}),$$

the null polarisation spectrum can only be obtained with the full sequence of four subexposures.

We assume throughout the paper that circular polarisation is *positive* for *right-hand* circularly polarised light, i.e. with an electric field vector rotating *clockwise* as seen by an observer *receiving* the radiation.

Altogether, in the case of our 1995 Dec. AAT observations, ESpRIT requires at least 128 MB of random access memory for optimal performance, and takes between 2 and 20 CPU minutes for processing a complete sequence of four subexposures, whether it runs on a new AlphaServer 600 or on an older Sparc 10 workstation.

4 LEAST-SQUARES DECONVOLUTION

4.1 Basic principles

As mentioned in the introduction, the Zeeman signatures we try to detect are extremely small, with typical relative amplitudes of 0.1% (Donati et al. 1992a). Detecting and inverting them in terms of a parent field distribution requires these signatures to be measured with high accuracy, i.e. with relative noise levels in Stokes V profiles lower than 10^{-4}. Clearly, one cannot get such low noise levels from a single line in a single spectrum (where we get at best relative noise levels of 10^{-3}). Moreover, as active stars rotate quite rapidly and may vary on timescales of a few rotations, one cannot phase-bin more than a few spectra to decrease the noise level to the required limit. A very interesting possibility is to extract the polarisation information from as many lines as possible in a single spectrum, as most lines are expected to exhibit Zeeman signatures with more or less the same shape. After the very encouraging results obtained from preliminary attempts in this direction (Semel & Li 1995; Carter et al.

1996), we present here a slightly more rigorous and sophisticated approach.

Assume a given magnetic configuration. In the weak field regime, each Stokes V local line profile obeys:

$$V_{\rm loc}(v) \propto g\lambda \frac{\partial I_{\rm loc}(v)}{\partial v}$$

where v represents the velocity coordinate $c\,\Delta\lambda/\lambda$ associated with a wavelength shift $\Delta\lambda$ from line centre wavelength λ, while g and $I_{\rm loc}(v)$ are respectively the magnetic sensitivity (Landé factor) and local profile of the selected line. Note that the proportionality factor is the same for all lines and only depends on the local longitudinal (i.e. line-of-sight projected) field value. If we now further assume that $I_{\rm loc}(v)$ is similar *in shape* for all lines and simply scales up in depth with the local line central depth d, we get:

$$V_{\rm loc}(v) = g\lambda d\ k_{\rm B}(v)$$

where $k_{\rm B}(v)$ is a proportionality function (equal for all lines). In principle, this second approximation is strictly valid only for optically thin lines. However, it is not too bad a model at the scale of a rotationally broadened line profile (typically tens of $\rm km\,s^{-1}$), provided very strong lines (like Balmer or Ca II H & K lines) are excluded. Integrating the previous equation over the whole rotating star (i.e. over all points M of brightness and radial velocity $b_{\rm M}$ and $v_{\rm M}$) gives:

$$\begin{aligned} V(v) &= \iint b_{\rm M}\ V_{\rm loc}(v - v_{\rm M})\ dS \\ &= g\lambda d \iint b_{\rm M}\ k_{\rm B}(v - v_{\rm M})\ dS \\ &= w\quad Z(v) \end{aligned}$$

If we finally assume wavelength-independent limb-darkening, the integral function $Z(v)$ – called mean Zeeman signature – is constant for all lines, and its shape is reproduced by all Stokes $V(v)$ profiles with a scaling factor $w = g\lambda d$.

Calling $M(v)$ the line pattern function defined by:

$$M(v) = \sum_i w_i\ \delta(v - v_i)$$

where v_i and w_i are respectively the position (in velocity space) and weight of each spectral line, the circularly polarised spectrum V can be written as a convolution expression ($V = M * Z$) or equivalently as a linear system ($\mathbf{V} = \mathbf{M}\cdot\mathbf{Z}$). Note that we further assume here that line intensities add up linearly which is clearly wrong, especially in the case of strongly saturated lines; in this very first attempt at using many lines together, we only account for this effect in a very rough way by ensuring that the sum of normalised central depths over nearby lines never exceeds 1. Looking for the least-squares solution in $\mathbf{Z}$ yields:

$$\mathbf{Z} = ({}^{\mathbf{t}}\mathbf{M}\cdot\mathbf{S^2}\cdot\mathbf{M})^{-1}\ \ {}^{\mathbf{t}}\mathbf{M}\cdot\mathbf{S^2}\cdot\mathbf{V} \quad (4)$$

where $\mathbf{S}$ notes the square diagonal matrix whose element S_{jj} contains the inverse error bar $1/\sigma_j$ of spectral pixel j (obtained directly from optimal extraction, see Sect. 3.3).

From this expression, those upset by all approximations made in the previous paragraphs can get a fresh view of what we actually do. The right hand part of Eq. 4 (denoted ${}^{\mathbf{t}}\mathbf{M}\cdot\mathbf{S^2}\cdot\mathbf{V}$) is actually a cross-correlation of the observed spectrum $\mathbf{V}$ with a line pattern $\mathbf{M}$, i.e. a *weighted* mean of all lines selected for the analysis. It is thus very similar in principle to what most other cross-correlation studies (like CORAVEL ones, e.g. Mayor 1980) do. The first result of the demonstration above is thus that it provides a built-in set of line weights w. The second is to yield a slightly more sophisticated result in the sense that we "clean" (i.e. deconvolve) the raw cross-correlation vector from the autocorrelation matrix ${}^{\mathbf{t}}\mathbf{M}\cdot\mathbf{S^2}\cdot\mathbf{M}$, and further, to provide a set of accurate error bars for the mean Zeeman signature $\mathbf{Z}$ (through the diagonal elements of the inverse autocorrelation matrix; see Press et al. 1992). The overall process is dubbed "Least-Squares Deconvolution" or LSD.

LSD also has a built-in automatic and iterative stray pixel rejection routine. Normally, most of these stray pixels (and in particular those due to cosmic ray hits) are discarded by optimal extraction. Our rejection routine will thus only get rid of the remaining ones, due for instance to dead CCD lines/columns or to cosmic ray hits affecting all pixels at a given wavelength within a given order. Note that both rejection processes are crucial here. The value of each spectral pixel in a LSD spectrum is typically computed from a few thousand different points in the original spectrum, each of these points corresponding to about one to two hundred CCD pixels (20 to 60 pxl per order and per sequence subexposure); the probability of getting one stray pixel within several hundred thousand being relatively high, efficient rejection is thus an absolute requirement here.

All LSD Zeeman signatures presented in the following section are scaled to a mean weight $w = g\lambda d$ of 500 nm, and are computed on a –240 to 240 $\rm km\,s^{-1}$ range with a spectral bin of 3 $\rm km\,s^{-1}$ (161 points altogether).

4.2 Performances

This method is of course particularly appropriate for polarisation spectra with a noise level in each individual line usually *larger* than the corresponding Zeeman signature. In this case, all approximations listed above – although very rough – do still represent a reasonable working assumption. As a matter of fact, the technique is found to work remarkably well, as one can judge from the results of Sect. 5. More unexpected is the finding that this technique also performs very well when applied to Stokes I spectra (using respective line weights equal to $w = d$) and can boost the sensitivity of Doppler imaging-like studies by a very large factor, as demonstrated in Donati & Cameron (1997). In the present study however, LSD Stokes I profiles (normalised to unit weight) are mainly presented for display purposes and essentially aim at demonstrating visually that the spectral location of Zeeman signatures and line profiles are indeed very well correlated.

The first task for LSD involves computing the reference line pattern $\mathbf{M}$. In CORAVEL terminology, $\mathbf{M}$ is called a *line mask*. For our application, digital masks have been computed for several model atmospheres ranging from A0 to M0 (see Table 2), with the help of Kurucz's atomic database, model atmosphere library (assuming a 2 $\rm km\,s^{-1}$ microturbulent velocity) and SYNTHE routines (Kurucz 1993). Landé factors are also taken from Kurucz's files whenever available (i.e. in 90% cases) and estimated from LS coupling otherwise. Central depths of intrinsic profiles are among the standard outputs in Kurucz's routines. Note that we only select

Table 2. Number of usable spectral lines (with central depth of intrinsic profile exceeding 40% of unpolarised continuum and located at least 50 $\mathrm{km\,s^{-1}}$ away from order edges) as a function of spectral type (i.e. effective temperature $T_{\rm eff}$) and spectral domain. The third column lists all available lines from 370 to 880 nm, while the next ones correspond to the smaller domains of each AAT run. The computations assume Kurucz LTE atmospheres with solar abundances and $\log g = 4$ (except for the Sun and the K0 model, with respective logarithmic gravities of 4.44 and 4.5). Note that these numbers are only given as an indication, and can vary in particular with stellar radial velocity (fixed here to 0 $\mathrm{km\,s^{-1}}$) and minimum requested distance from order edges.

Spectral type	$T_{\rm eff}$	Total	1991 Aug.	1991 Dec.	1992 Dec.	1993 Dec.	1995 Dec.
A 0 IV	10,000	254	7	8	8	23⋆	33
A 4 IV	8,500	868	51	50	74	99⋆	203
F 1 IV	7,000	1,986	149	150	222	222	576
F 6 IV	6,250	2,880	231	233	351	355	902
Sun	5,777	4,170	363	372	582	591	1,472
G 2 IV	5,750	3,761	333	339	523	531	1,286
G 7 IV	5,250	4,840	438	448	694	710	1,748
K 0 V	5,000	5,038	442	452	714	728	1,801
K 1 IV	4,750	5,843	513	529	835	854	2,095
K 5 IV	4,250	6,535	555	568	914	931	2,285
M 0 IV	3,750	5,921	455	459	754	771	1,896

⋆These numbers correspond to the second bluer setup (see Table 1)

lines whose local depth exceeds 40% (in units of unpolarised continuum) in order not to overrepresent the weak line class in the list. Computing one mask takes typically 1 CPU hr on an average Dec Alpha workstation. We then extract a sublist from the full mask, according to the available spectral domain in the observations (once order edges are trimmed).

For a K1 star, the total number of lines available in our AAT observations vary from about 500 (in 1991) to over 2,000 in 1995 (see Table 2). Note that most lines are severely blended (especially for rapid rotators) and this is precisely why we have to use so many at the same time; while the coherent signal progressively builds up, the incoherent photon noise and blending contamination decreases with respect to the main signal. One obvious property of LSD is that it is equally efficient at *all stellar rotation rates*, as verified in Sect. 5 for stars with line-of-sight projected rotational velocities of up to 160 $\mathrm{km\,s^{-1}}$. It therefore represents a particularly interesting option for studying surface inhomogeneities on ultra fast rotators, usually out of reach of conventional tomographic techniques known to suffer from line blending problems at very high rotation rates.

When Least-Squares Deconvolving Stokes V profiles, photon noise dominates blending pollution; as expected, we observe that S/N ratios in mean profiles⋆ roughly increase (with respect to a single line with average magnetic sensitivity) as the square root of the total number of available lines in the selected mask (see Fig. 1). Note that the multiplex gains we obtain (defined as the ratio of S/N in LSD polarised profiles to the *peak* S/N in the original Stokes V spectra) do not exactly follow this square-root relation. This point is essentially due to the fact that S/N is *not* constant throughout the recorded spectra; the greater the wavelength coverage (i.e. the more lines recorded), the less representative (for the overall spectrum quality) is the *peak* S/N ratio, so the further multiplex gains end up below the pure square-root relation. The values we obtain do nevertheless correspond to the theoretical upper limit *given the uneven S/N in the recorded spectra*, implying that our implementation of LSD is close to optimal as far as global efficiency is concerned.

⋆ In the following text, we define S/N of Stokes V spectra as $1/n$ where n is the relative noise level per digital channel. Being roughly equal to the square root of the total number of photons collected in the corresponding bin, this parameter is thus nothing more than a polarisation spectrum quality indicator, and gives in particular no information about the accuracy to which a potential Zeeman signature may be detected.

When using about 2,000 spectral features simultaneously (in the particular case of a K1 star observed in 1995 Dec.), we obtain a net sensitivity increase of up to 7.5 mag in flux compared to a single "average" line analysis. This efficiency increase exceeds 4.5 mag in flux with respect to the old three-line technique of Donati et al. (1992a); although 2.3 times more magnetically sensitive (i.e. $2.3^2 = 5.3$ times more efficient) than our average line each, the three previously selected features are indeed still altogether about 65 times *less* efficient in flux than the full sample we use now (see Fig. 2).

Note that such multiplex gains only apply for LSD of polarisation spectra. Although LSD of Stokes I spectra also performs quite well, it often turns out to be less efficient than its Stokes V equivalent; if we exclude very weakly exposed stellar spectra, the dominant noise in the resulting unpolarised profiles is indeed essentially due to the blending effect of neighbouring spectral lines that are inaccurately modelled (and sometimes even not included) in the computed spectral masks and/or the convolution process, rather than to photon noise as for polarisation spectra (see Donati & Cameron 1997 for a more quantitative description in the particular case of the ultra fast rotator AB Doradus). For very faint objects however, LSD of Stokes I spectra is expected to be just as efficient as its Stokes V equivalent, with multiplex gain in S/N as much as a few tens for K1 objects.

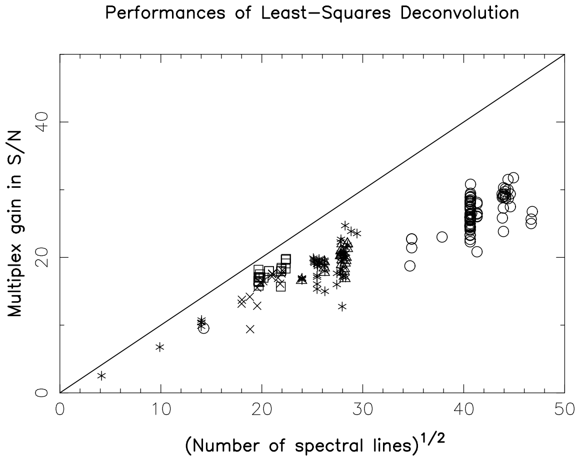

Figure 1. Multiplex gain in S/N as a function of the square root of the number of spectral lines used in Least-Squares Deconvolution. Different observing runs are noted with different symbols (× for 1991 Aug., 2 for 1991 Dec., △ for 1992 Dec., $*$ for 1993 Dec. and ◯ for 1995 Dec.). The full line depicts the theoretical upper limit.

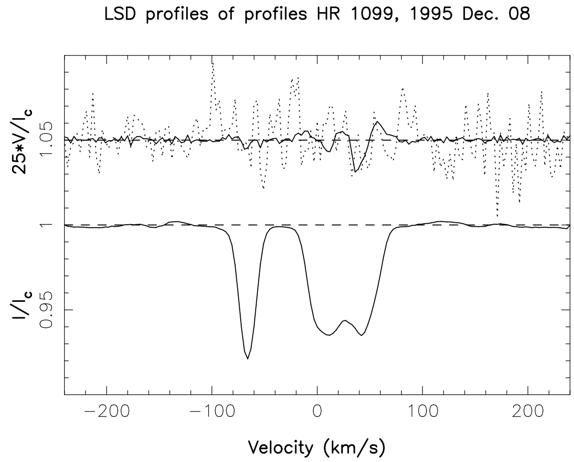

Figure 2. LSD unpolarised (bottom curve, full line) and circularly polarised (top curve, full line) profiles of HR 1099 (on 1995 Dec. 08). Compared to the old three-line analysis of Donati et al. (1992a) whose application on the same data yields the dotted curve, we obtain a net sensitivity increase in flux of about 4.5 mag without which the Zeeman signature could not have been detected. Note that the polarisation profiles are expanded by a factor of 25 and shifted upwards by 1.05 for display purposes.

4.3 Detection diagnoses

The statistical test we use to diagnose the presence of a signal in either mean V or mean N profiles is essentially the same as that of Donati et al. (1992a). We compute the reduced χ^2 test statistics inside and outside spectral lines (whose location is derived from LSD unpolarised profiles) for both V and N profiles, and convert these values into detection probabilities (given the number of pixels on which the reduced χ^2 are estimated). In this paper, we consider that a signal is unambiguously detected in either V or N whenever the associated probability is larger than 99.999% (i.e. false alarm probability smaller than 10^{-5}), that marginal evidence for a signature is obtained if the false alarm probability is larger than 10^{-5} but smaller than 10^{-3}, and that no signal is observed otherwise. Note that a true signature can still be either real polarisation (and thus indicate a magnetic detection) or spurious information in case of an instrumental problem (see Sect. 5.1.1); however, checking that a signal is detected only in V and not in N, and that it is located within the line profile velocity interval (i.e. $v_{\rm rad} - v \sin i$ to $v_{\rm rad} + v \sin i$ essentially, $v_{\rm rad}$ noting the stellar radial velocity and $v \sin i$ the line-of-sight projected rotation velocity at the stellar equator) enables us to conclude that it corresponds to true polarisation.

Whenever detected with sufficient accuracy, LSD Zeeman signatures can also be used to extract additional information on the physical properties of the corresponding stellar magnetic regions, and in particular on their temperature contrast with respect to the surrounding photosphere. The amplitude of the polarisation signal depends indeed on the temperature of the associated magnetic regions, through both local continuum brightness on one hand *and* mean profile equivalent width on the other hand. If the magnetic region is cooler than the photosphere, the spot-to-photosphere brightness ratio is larger in the red than in the blue. Similarly, going from a e.g. 5000 K photosphere to a 3500 K spot generates a stronger decrease of the mean Stokes I profile equivalent width in the blue than in the red (this is indeed what we get from partial blue and partial red LSD unpolarised spectra of the slowly rotating K0V and M4V template stars Gl 176.3 and Gl 367). Altogether, we thus expect mean Stokes V signatures to be smaller in the blue than in the red for a cool magnetic spot. A similar argument (using the solar spectrum as a G2V template) yields an opposite conclusion for a warm magnetic plage.

To quantify this point a bit more, we constructed two K0V submasks, one including all spectral lines bluer than 500 nm (centred on 480 nm), the other one including those redder than 550 nm (centred on 610 nm). Apart from a population difference (partly compensating the higher S/N values in the red part of the spectrum), the two samples are statistically identical within 10%, as far as overall magnetic sensitivity, mean line depth, mean excitation potential and mean Landé factor are concerned. Moreover, the slight difference in overall magnetic sensitivity is corrected by an adequate scaling of the Zeeman signature (see Sect. 4.1). Assuming that the continuum brightness obeys the Planck function, we estimate that a 1,500 K temperature deficit within the magnetic region should generate a blue Stokes V signature whose size is 63% smaller than the red one, while a 750 K excess should make it 25% larger. Although strictly valid for a K0V atmosphere only, these values can be still be used as guidelines for most cool active objects studied in this paper.

5 RESULTS

Two-hundred and twenty nine polarisation spectra were recorded for 21 active stars and 7 calibration objects throughout our 5 AAT runs. Information about the programme stars, whose evolutionary status ranges from pre-main sequence to red giant branch stage, can be found in Table 3. Table 4 lists the journal of observations. In partic-

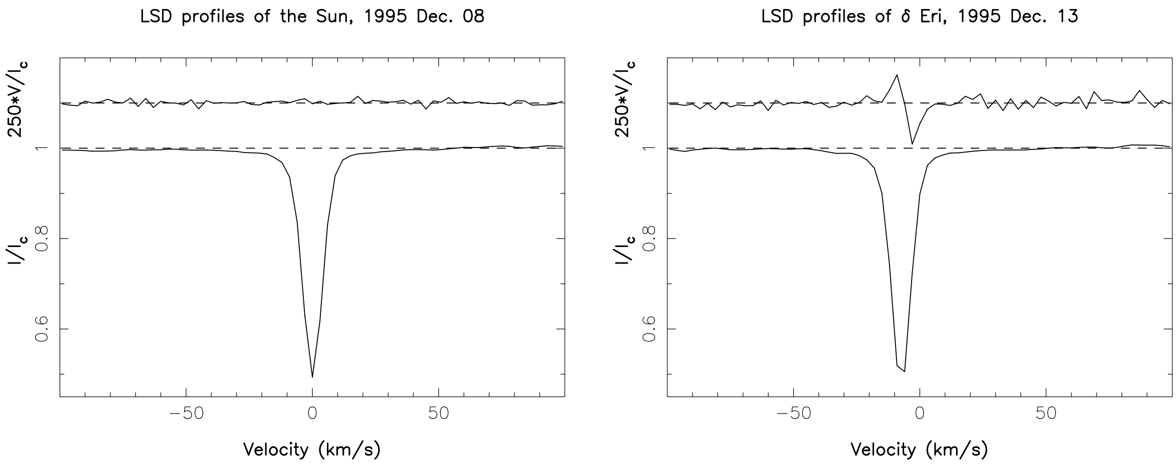

Figure 3. LSD unpolarised (bottom curve of each panel) and circularly polarised (top curve of each panel) profiles, for the Sun on 1995 Dec. 08 (left panel) and the inactive K1 star δ Eri on 1995 Dec. 13 (right panel). Note that the residual circular polarisation signature is expanded 250 times, i.e. 10 times more than in all similar plots.

ular, the S/N ratio for each LSD spectrum (along with the associated multiplex gain) is indicated.

5.1 Test stars

Polarisation standards are used to check the correct behaviour of both instrumentation and data processing.

5.1.1 The Sun and the inactive K1 star δ Eri

Since circular polarisation in line profiles is almost absent in disc integrated light from the Sun or from other similar weakly active stars, and cannot be generated by optical transmission through the instrument, we expect to detect no Zeeman signatures for these objects, up to a very high accuracy level. Observing these targets thus provides a very good way of checking the correct behaviour of both observing procedure and reduction package. In particular, we can look for possible sources of spurious polarisation signals (stellar rotation and variability, Earth rotation, drifts in the spectrograph, inhomogeneities in CCD pixel sensitivities...) that may result from the fact that both polarisation states are not (and cannot be) recorded at the same time, on the same CCD pixels and through the same instrument channel. As illustrated on Fig. 3, observations show that no spurious polarisation signatures are detected down to a relative noise level of 2×10^{-5}), except in one single occasion (δ Eri on 1995 Dec. 13) where a polarisation artifact of about 6×10^{-4} is measured. To understand its origin, we must remember (following Semel et al. 1993) that small residual velocity shifts Δ do exist between the two orthogonally polarised spectra of each subexposure (due to small calibration errors when correcting slit direction and shape), as well as global shifts from one subexposure to the next (denoted by δ and due to possible Doppler shifts and/or spectrograph drifts). Global time variations *in shape* of the normalised spectrum I from one subexposure to the next (due to potential fluctuations in the fibre illumination), as well as slight differences *in shape* between the two normalised spectra of each subexposure (noted dI and due to differential optical aberrations inside the spectrograph), must also be taken into account. Observations show that all such effects are small; if $\Delta\ \partial I/\partial v$ and $\delta\ \partial I/\partial v$ usually do not exceed 10^{-2}, dI and $t\ \partial I/\partial t$ (t denoting the time interval between two successive subexposures) are at most half as large. Assuming that the true polarisation signal P is equal to zero, a second order Taylor expansion of Eqs. 1 and 2 yields the following analytical expression for the residual *spurious* polarisation signature s:

$$s = \frac{1}{4}\left[I\ h\Big(\frac{dI}{I}\Big) + \Delta\left(\frac{\partial h}{\partial v} - \frac{h}{I}\frac{\partial}{\partial v}\right)(I)\right]$$

where h notes the first order differential $\delta\ \partial/\partial v + t\ \partial/\partial t$ describing the overall time variation of the normalised spectrum (in both wavelength *and* shape) between two successive subexposures. As demonstrated already by Semel et al. (1993), all first order terms cancel out in the calculation and are therefore absent from the above expression. Altogether, we find that s should always be smaller that 10^{-4}, in contradiction to what we observe for δ Eri on 1995 Dec. 13 (Fig. 3, right panel).

To explain this point, we must take into account possible time variations of Δ (due to internal instabilities of the spectrograph or even simply photon noise, ignored in Semel et al.'s first order estimation) between two successive subexposures by a typical amount Δ'. We then obtain a new expression for s:

$$s' = s + \frac{1}{4}\Delta'\frac{\partial I}{\partial v}.$$

Although $\Delta'\ \partial I/\partial v$ is usually about twenty times smaller than $\Delta\ \partial I/\partial v$, with typical values of 0.5×10^{-3}, it can grow as large as 2.5×10^{-3} and thus generate spurious polarisation signatures of up to 6×10^{-4}. A detailed look at the problematic δ Eri observation confirms this interpretation, the associated internal spectrograph instabilities we measure in this case reaching up to 5×10^{-3} pxl or 15 m s^{-1}. In all other observations, spectrograph instabilities are about 3 to 5 times smaller, i.e. in the 3 to 5 m s^{-1} range. Although small, these fluctuations are clearly larger than the photon noise limit (given the high S/N values obtained on the Sun and δ Eri, ranging from 360 to over 1,000 for each subexposure, see Table 4) and must therefore be attributed to an

Table 3. List of programme stars. All $v \sin i$ values are obtained from LSD unpolarised spectra.

Object	HD number	m_V (mag.)	Spectral type	Mask used	$v \sin i$ (km s^{-1})	Period (d)
Calibration objects: *"Non magnetic" standards*						
Sun			G2V	Sun		
δ Eri	23249	3.5	K1IV	K1		
Magnetic standards (magnetic Cp stars)						
HD 37776	37776	7.0	B2p		< 110	1.53869
HD 54118	54118	5.2	A0p		34	3.27533
HR 2727	55719	5.3	A3p			36.48
HD 94660	94660	6.1	A0p			
HD 175362	175362	5.4	B6p		< 38	3.67375
Young objects: *T Tauri stars*						
SU Aur	282624	9.1	G2IV	G2	59	3.094
V410 Tau	283518	10.8	K2IV	K1	72	1.871
HD 283572	283572	8.6	G8IV	G7	77	1.548
FU Ori stars						
FU Ori		8.9	G3	G2		
Herbig stars						
HD 100546	100546	6.8	B9V	A0	65	
HD 104237	104237	6.6	A4V	A4	12	
ZAMS stars						
AB Dor	36705	6.8	K0V	K0	91	0.51479
LQ Hya	82558	7.8	K0V	K0	27	1.6011
HD 155555	155555	6.7	G5IV/K0IV	G7	34/32	1.681652
Main sequence objects: *Low mass flare stars*						
CC Eri	16157	8.7	K7–9V	K5	17	1.56145
Early-type active stars						
α Hyi	12311	2.9	F0V	F1	158	
Evolved objects: *RS CVn binaries*						
CF Tuc	5303	7.6	G0V/K4IV	K5	25/70	2.79767
HR 1099	22468	5.7	G5IV/K1IV	K1	12/41	2.83774
EI Eri	26337	7.1	G5IV	G7	51	1.947227
TY Pyx	77137	6.9	G5IV/G5IV	G7	27/28	3.198584
IL Hya	81410	7.9	K1III/	K1	25/	12.908
42 Cap	206301	5.2	G2IV/	G2		13.1740
IM Peg	216489	5.6	K2III	K1	25	24.65
SZ Psc	219113	7.4	F8IV/K1IV	K1	/71	3.965703902
II Peg	224085	7.4	K2IV	K1	22	6.724183
FK Com stars						
YY Men	32918	8.4	K1III	K1	45	9.5476

instrumental problem, whose exact origin still needs to be worked out.

One must keep in mind anyway that such spurious signatures, already extremely small, will be considerably smaller for most rapid rotators we usually focus on. Due to rotational broadening, disc integrated spectral lines can indeed get three to ten times shallower than their equivalent on the Sun and δ Eri, while their first and second derivatives with wavelength are decreased by a factor of ten to a hundred. Moreover, we can check from the analytical expression of s' that this effect roughly compensates potentially larger Doppler shifts (for close binary stars) or spectral distortions (due for instance to rotational modulation) between successive subexposures, as long as t is reasonably short compared to both orbital and rotational periods. We thus conclude that spurious polarisation signatures should be smaller than 10^{-4} peak-to-peak for all of our primary targets. This fact can be verified experimentally by looking at LSD null po-

Table 4. Journal of observations. For each star, we list here the observing date (second column), the number of exposure sequences collected on this object at this date ($n_{\rm exp}$, third column), together with the range of corresponding Julian dates (fourth column), total exposure times ($t_{\rm exp}$, fifth column) and *peak* S/N ratios per 3 $\rm km\,s^{-1}$ pxl (sixth column). The two last columns indicate respectively the range of S/N ratios in the associated LSD spectra and the corresponding multiplex gains in S/N (whenever available).

Object	Date	$n_{\rm exp}$	JD (2,400,000+)	$t_{\rm exp}$ (sec.)	S/N ($\rm pxl^{-1}$)	$\rm S/N_{LSD}$ ($\rm pxl^{-1}$)	Multiplex gain
Sun	1991 Aug. 19	1	48487.8494	360	1360	12800	9
Sun	1991 Aug. 20	1	48488.8509	300	1480	21000	14
Sun	1992 Dec. 09	1	48966.1479	240	2940	47600	16
Sun	1992 Dec. 10	1	48967.1546	240	2530	42000	17
Sun	1993 Dec. 25	1	49346.9840	120	1450	24200	17
Sun	1993 Dec. 26	1	49347.9746	120	1390	23400	17
Sun	1993 Dec. 27	1	49349.1149	120	1620	27400	17
Sun	1993 Dec. 28	1	49350.1263	120	2020	34300	17
Sun	1993 Dec. 29	1	49351.1408	120	1840	31100	17
Sun	1995 Dec. 08	1	50060.0703	240	2120	48800	23
δ Eri	1992 Dec. 09	1	48966.1319	480	1070	22800	21
δ Eri	1992 Dec. 10	1	48967.1432	480	830	18300	22
δ Eri	1992 Dec. 11	1	48968.1865	480	1010	22200	22
δ Eri	1993 Dec. 24	1	49346.1250	480	1710	37300	22
δ Eri	1995 Dec. 13	1	50064.9706	240	790	25100	32
HD 37776	1993 Dec. 25	1	49347.1396	1200	580		
HD 37776	1993 Dec. 26	1	49348.1355	1200	230		
HD 37776	1993 Dec. 27	1	49349.1271	1200	410		
HD 37776	1993 Dec. 28	1	49350.1405	1200	560		
HD 37776	1993 Dec. 29	1	49351.1534	1200	490		
HD 54118	1991 Dec. 18	1	48609.2075	1200	450		
HR 2727	1992 Dec. 10	3	48967.1721/48967.2118	1200	720/860		
HD 94660	1992 Dec. 11	1	48968.2612	2400	670		
HD 94660	1993 Dec. 28	1	49350.2556	1200	880		
HD 94660	1993 Dec. 29	1	49351.2497	1200	800		
HD 94660	1995 Dec. 08	1	50060.2452	480	200		
HD 175362	1991 Aug. 18	1	48487.1212	2400	830		
HD 175362	1991 Aug. 19	3	48487.9554/48487.9912	1200	660/710		
SU Aur	1995 Dec. 12	2	50064.0593/50064.0762	2400	110	2500	23
SU Aur	1995 Dec. 13	1	50065.0595	2400	84	1800	21
V410 Tau	1993 Dec. 25	1	49347.0049	2400	330	3000	9
V410 Tau	1993 Dec. 27	1	49348.9959	1800	100	1600	16
V410 Tau	1993 Dec. 28	1	49350.0014	3600	160	2900	18
V410 Tau	1993 Dec. 29	1	49351.0108	3600	170	2900	17
HD 283572	1993 Dec. 25	1	49347.0396	2400	300	5800	19
HD 283572	1993 Dec. 26	2	49348.0025/49348.0484	3600	150/200	2800/3800	19
HD 283572	1993 Dec. 27	1	49349.0245	2400	240	4100	17
HD 283572	1993 Dec. 28	2	49350.0402/49350.0710	2400	300	4600/5200	15/17
HD 283572	1993 Dec. 29	2	49351.0499/49351.0820	2400	280	4500/5300	16/19
FU Ori	1995 Dec. 08	1	50060.0449	2400	160	3000	19
HD 100546	1993 Dec. 29	1	49351.1915	2400	750	1900	3
HD 104237	1993 Dec. 29	1	49351.2237	2400	740	5000	7
HD 104237	1995 Dec. 12	2	50064.2485/50064.2568	1200	210/220	2000/2100	10
AB Dor	1991 Dec. 17	6	48608.1042/48608.2024	1200	220/240	3800/4200	17/18
AB Dor	1991 Dec. 18	5	48609.1095/48609.1821	1200	100/140	1700/2300	16/17
AB Dor	1995 Dec. 07	19	50058.9145/50059.2509	800	230/380	5900/10400	26/29
AB Dor	1995 Dec. 10	2	50062.2464/50062.2570	400/800	86/150	2000/3400	23
AB Dor	1995 Dec. 11	26	50062.9291/50063.2649	800	130/310	2900/7500	22/27
AB Dor	1995 Dec. 12	3	50063.9063/50063.9302	800	250/270	7700/7900	29/31
AB Dor	1995 Dec. 13	3	50064.9033/50064.9273	800	190/200	5600/5800	29
LQ Hya	1991 Dec. 17	1	48608.2353	3000	300	5400	18
LQ Hya	1991 Dec. 18	1	48609.2320	2400	250	4500	18
LQ Hya	1992 Dec. 09	1	48966.2340	4800	460	8900	19
LQ Hya	1992 Dec. 10	1	48967.2459	3600	640	11800	18
LQ Hya	1992 Dec. 11	1	48968.2196	3600	450	8000	18
LQ Hya	1993 Dec. 24	1	49346.2337	4800	790	14200	18
LQ Hya	1993 Dec. 25	1	49347.2323	2400	720	14000	19
LQ Hya	1993 Dec. 26	1	49348.2336	866	140	2100	15
LQ Hya	1993 Dec. 27	2	49349.2194/49349.2512	2400	460/480	8700/9000	19

Table 4. (continued)

Object	Date	$n_{\rm exp}$	JD (2,400,000+)	$t_{\rm exp}$ (sec.)	S/N ($\rm pxl^{-1}$)	$\rm S/N_{LSD}$ ($\rm pxl^{-1}$)	Multiplex gain
LQ Hya	1993 Dec. 28	1	49350.2380	1200	500	9800	20
LQ Hya	1995 Dec. 08	3	50060.1497/50060.2191	2400	320/460	9000/12000	26/28
LQ Hya	1995 Dec. 12	3	50064.1103/50064.2216	2400	230/250	6100/6600	26/27
LQ Hya	1995 Dec. 13	1	50065.0931	1200	48	1000	21
HD 155555	1991 Aug. 19	1	48487.9079	4800	740	12200	16
HD 155555	1991 Aug. 20	2	48488.8770/48488.9174	2400	400/410	6500/6700	16
HD 155555	1991 Aug. 27	2	48495.8816/48495.9183	2400/3000	210/380	2700/5900	13/16
CC Eri	1995 Dec. 12	2	50063.9811/50063.9979	1200	200/230	5000/5900	25/26
CC Eri	1995 Dec. 13	1	50064.9912	2400	310	8300	27
α Hyi	1993 Dec. 27	2	49348.9036/49348.9115	160/240	1090/1260	11300/12400	10
α Hyi	1993 Dec. 28	1	49349.9088	240	1390	14500	10
α Hyi	1993 Dec. 29	1	49350.9072	240	1460	15700	11
CF Tuc	1993 Dec. 27	1	49348.9326	2400	510	12000	24
CF Tuc	1993 Dec. 28	1	49349.9274	2400	390	9300	24
CF Tuc	1993 Dec. 29	1	49350.9272	2400	510	12600	25
HR 1099	1991 Aug. 19	2	48488.2607/48488.3156	3600/4800	940/1100	17000/19400	18
HR 1099	1991 Aug. 20	1	48489.3034	4800	630	10700	17
HR 1099	1991 Dec. 16	2	48607.0221/48607.1204	3908/4800	510/520	8000/9500	16/18
HR 1099	1991 Dec. 17	3	48607.9671/48608.0711	2400/4800	730/1040	13100/18700	18
HR 1099	1991 Dec. 18	3	48608.9523/48609.0559	2400/4800	310/670	6100/12300	18/20
HR 1099	1992 Dec. 09	5	48965.9952/48966.1731	2400	500/1180	11000/23900	20/22
HR 1099	1992 Dec. 10	3	48966.9840/48967.0996	2400/4800	1290/1940	26100/36700	19/21
HR 1099	1992 Dec. 11	4	48967.9847/48968.1639	2400/4800	680/1900	12200/36400	17/19
HR 1099	1992 Dec. 12	1	48968.9826	2400	560	11000	20
HR 1099	1993 Dec. 24	4	49345.9329/49346.1009	2400	1010/1400	22900/31200	18/23
HR 1099	1993 Dec. 25	4	49346.9297/49347.1100	2400	1460/1670	18600/31900	13/21
HR 1099	1993 Dec. 26	2	49347.9217/49347.9535	2400	890/950	18200/19100	20
HR 1099	1993 Dec. 27	3	49348.9668/49349.0952	2400	1190/1230	23100/25000	19/21
HR 1099	1993 Dec. 28	2	49349.9601/49350.1084	2400	1380/1490	24300/29800	18/20
HR 1099	1993 Dec. 29	2	49350.9686/49351.1215	2400	1220/1340	20800/26800	17/20
HR 1099	1995 Dec. 07	1	50058.9006	800	480	14100	29
HR 1099	1995 Dec. 08	7	50059.9137/50060.1158	1200	470/750	11200/21800	24/30
HR 1099	1995 Dec. 09	1	50061.0159	600	360	9300	26
HR 1099	1995 Dec. 11	1	50063.1525	1200	400	11000	28
HR 1099	1995 Dec. 12	4	50063.9462/50064.1537	1200	370/620	10100/17900	27/29
HR 1099	1995 Dec. 13	2	50064.9426/50064.9593	1200	530/570	15400/16400	29
EI Eri	1993 Dec. 24	1	49346.1467	2400	700	13500	19
EI Eri	1993 Dec. 26	1	49348.1099	2400	390	7500	19
TY Pyx	1993 Dec. 24	1	49346.1854	2400	830	16400	20
TY Pyx	1993 Dec. 25	2	49347.1651/49347.1977	2400	1010/1030	19700/20300	20
TY Pyx	1993 Dec. 26	2	49348.1618/49348.2096	2190/2400	350/420	6700/8100	19
TY Pyx	1993 Dec. 27	1	49349.1550	2400	660	12900	20
TY Pyx	1993 Dec. 28	1	49350.1652	2400	940	18700	20
IL Hya	1993 Dec. 27	1	49349.1869	2400	570	11800	21
IL Hya	1993 Dec. 28	1	49350.1982	2400	840	18000	21
42 Cap	1991 Aug. 19	1	48488.0215	2400	1200	16500	14
42 Cap	1991 Aug. 20	1	48489.0075	2400	410	5400	13
IM Peg	1991 Dec. 17	1	48607.9197	1800	460	9100	20
SZ Psc	1991 Aug. 19	3	48488.0648/48488.1652	3600	460/590	7900/10400	17/18
SZ Psc	1991 Aug. 20	1	48489.1654	3600	180	2900	16
II Peg	1992 Dec. 10	1	48966.9324	3600	630	12300	20
II Peg	1992 Dec. 11	1	48967.9342	2400	260	5200	20
YY Men	1995 Dec. 08	1	50060.0059	2400	200	6000	30
YY Men	1995 Dec. 12	1	50064.0241	2400	230	6600	29
YY Men	1995 Dec. 13	1	50065.0251	2400	200	6300	32

larisation spectra N (see Sect. 3.4) and checking that no signal is detected (according to the definition of Sect. 4.3). This is indeed what we observe (see Fig. 20 in Sect. 5.4.4 for an example) whenever the global time variation of the polarisation rate P/I (due to either orbital motion, rotational modulation or true intrinsic variability) is not too large within the exposure sequence, the first order Taylor expansion of N *in presence of a polarisation signal* being equal to 0.5 I $h(P/I)$ (see Eqs. 1 and 3).

5.1.2 Magnetic chemically peculiar stars

Magnetic chemically peculiar (Cp) stars (whose extensively studied large scale fields are presumably stable on timescales of at least several decades) are observed on each run to check that the polarisation rates and signs we obtain are in good agreement with previously published results. The five objects we looked at throughout our 5 AAT runs are HD 37776, HD 54118, HR 2727, HD 94660 and HD 175362. For the coolest ones (i.e. HR 2727, HD 54118 and HD 94660), two special line masks were computed (for spectral types A4 and A0) to try to account (at least in a rough way) for their atmospheric peculiarities; while microturbulence was set to 0 $\mathrm{km\,s^{-1}}$, the metallic abundance we used is 10 times solar except for Cr (100 times solar), Ca and Sc (solar) – typical to what is observed on similar well known cool Ap stars like 53 Cam (Landstreet 1988) or 73 Dra (Babel & North 1997). For the two hottest objects (HD 175362 and HD 37776), two additional line masks were produced from B6 (16,000 K) and B2 (23,000 K) LTE model atmospheres respectively, assuming 0 $\mathrm{km\,s^{-1}}$ microturbulence and solar abundances. Note that this analysis, although rough, should be sufficient for our particular purpose, i.e. demonstrating that the LSD Stokes V signatures we recover for these objects are compatible with previously published longitudinal field estimates.

HD 54118 was observed only once on 1991 Dec. 18. The corresponding rotational phase (from the ephemeris of Bohlender et al. 1993) is 0.83±0.03 (phase 0.0 referring to longitudinal field maximum). The LSD Stokes I profile we obtain is strongly asymetric and indicate a line-of-sight projected rotational velocity $v \sin i$ of 34 ± 2 $\mathrm{km\,s^{-1}}$, while the LSD Stokes V profile exhibits a typical crossover signature as expected from the rotational phase at which the object was observed. The corresponding longitudinal field estimate B_ℓ (in G) can be obtained from both LSD Stokes I and V profiles with the following equation:

$$B_\ell = 2.14 \times 10^{11} \, \frac{\int \, vV(v) \, dv}{\lambda \, g \, c \int \, (1 - I(v)) \, dv} \qquad (5)$$

where g and λ (in nm) refer to *average* Landé factor and wavelength of all spectral features involved in the LSD process. The value we derive for HD 54118 (from LSD on 66 spectral features simultaneously) is equal to $B_\ell = 710 \pm 80$ G, in very good agreement with Bohlender et al.'s (1993) results.

HD 94660 belongs to the small class of Ap stars with resolved Zeeman split lines (Mathys 1990). Four spectra of this object were recorded, on 1992 Dec. 11, 1993 Dec. 28 and 29, and 1995 Dec. 08, all yielding (from LSD deconvolution of 91 to 230 spectral features simultaneously, depending on the epoch) a longitudinal field value of $B_\ell = -1820 \pm 90$ G, in very good agreement with accurate estimates by Mathys (1991) and Mathys & Hubrig (1997). In particular, it confirms that rotational modulation of the longitudinal field of HD 94660 is very weak. A new observational fact to report about this star is that its radial velocity is variable (we measure values of 1.8, 25.2, 25.2, 33.9 $\mathrm{km\,s^{-1}}$ with error bars of less than 1 $\mathrm{km\,s^{-1}}$ for each of the epochs mentioned above), as independently confirmed by Mathys et al. (1997) in a very recent study. Moreover, although the *shape* of most line profiles is only very weakly variable (just as the longitudinal field itself), a dramatic profile variability is observed for a few spectral lines, like for instance the unidentified feature at 563.356 nm whose equivalent width almost doubled between 1992 Dec. 11 and 1995 Dec. 08.

HR 2727 is a double-line spectroscopic binary (Bonsack 1976) whose Ap component also features resolved Zeeman split lines (Mathys 1990). The mean field modulus of this component, as estimated from the resolved Zeeman split lines, is rotationally modulated with a period of about 800 d (Mathys et al. 1997). The present observations (three spectra recorded on 1992 Dec. 10) occur at orbital phase 0.452 (according to Bonsack's ephemeris), which agrees well with the radial velocity we measure for the Ap star (32.8 $\mathrm{km\,s^{-1}}$). Our first spectrum corresponds to circular polarisation. Thanks to the lower effective temperature of HR 2727, up to 312 spectral features could be used simultaneously for LSD, yielding a longitudinal field value of $B_\ell = 810 \pm 100$ G. This is compatible with Mathys & Hubrig's (1997) recent estimates from spectra that bracket our observation in time within about 90 d, i.e. $\simeq 11\%$ of the rotational cycle). Our two last spectra were recorded in linear polarisation (Stokes Q and U respectively) with the special observing procedure described in Sect. 2. The first conclusion of this experiment is that crosstalk from circular to linear polarisation is very small (contamination from V to Q and U smaller than 1% of V), and that the efficiency at detecting circular polarisation is therefore maximum. The second interesting conclusion is that linear polarisation signatures are fairly small; in the very strong 492.3927 nm Fe II line (Landé factor of 1.7), the total linear polarisation signal does not exceed 1.5% peak-to-peak, i.e. five times smaller than the overall circular polarisation signature.

Four observations of the He weak star HD 175362 were obtained on 1991 Aug. 18 (one Stokes V spectrum) and on 1991 Aug. 19 (one Stokes V, one Stokes Q and one Stokes U exposures). The corresponding rotational phases are 0.00±0.03 and 0.22±0.03 for Aug. 18 and 19 respectively (Mathys 1991). HD 175362 being significantly hotter than the previous objects, there is only a dozen spectral features available for LSD. The amount of spectral line broadening as measured from LSD Stokes I profiles is 38 $\mathrm{km\,s^{-1}}$. As the surface field is rather strong on this object (and thus contributes significantly to the overall width of spectral lines, see Mathys & Hubrig 1997), this broadening estimate can only be considered as an upper limit for $v \sin i$. LSD Stokes V observations yield longitudinal field values of -3740 ± 200 G and -2400 ± 290 G for each rotational phase respectively, i.e. totally compatible with earlier measurements by Mathys (1991). Stokes Q and U observations of HD 175362 bring us to the same conclusions as those reached for HR 2727.

In 1993, five circularly polarised observations of the He rich star HD 37776 were obtained between Dec. 25 and Dec. 29, at a rate of one spectrum per night. The corresponding phases are 0.25, 0.90, 0.55, 0.21 and 0.86 according to Thomson & Landstreet's (1985) ephemeris, with a global phasing uncertainty of ±0.11 cycle. Due to the high effective temperature of HD 37776, only 17 spectral features could be used for LSD. The total line broadening we observe on the LSD Stokes I profile, about 110 $\mathrm{km\,s^{-1}}$, can only be considered as an upper limit for $v \sin i$ as some of this broadening is very likely attributable to the very strong surface field of this object. The longitudinal field estimates we obtain from LSD

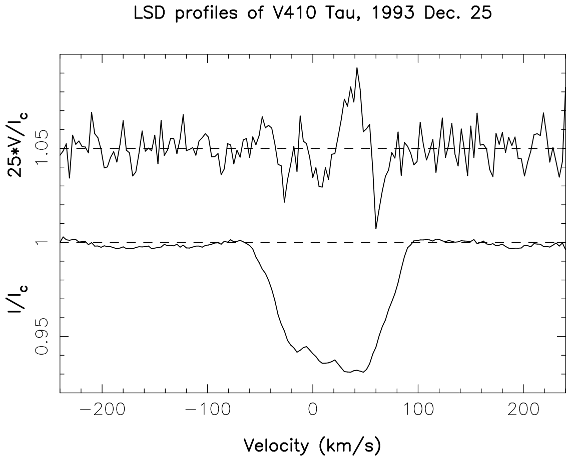

Figure 4. LSD unpolarised (bottom curve) and circularly polarised (top curve) profiles, for the weak-line T Tauri star V410 Tau on 1993 Dec. 25. Note that the mean polarisation profiles are expanded by a factor of 25 and shifted upwards by 1.05 for obvious display purposes.

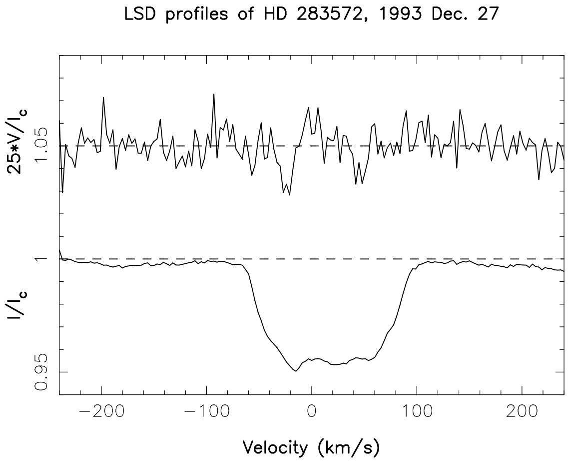

Figure 5. Same as Fig. 4 for the weak-line T Tauri star HD 283572 on 1993 Dec. 27

Stokes V profiles are equal to -1030 ± 170 G, 110 ± 360 G, -1090 ± 290 G, -1240 ± 170 G and -840 ± 200 G for each phase respectively, in excellent agreement with Bohlender's (1988) results.

As a summary to this section, we can conclude that our polarimeter behaves properly and yields magnetic field values in good agreement with those published to date in the literature. In particular, it indicates that that ZDI from LSD Stokes V profiles should not suffer from systematic flux over or underestimation problems similar to those reported in Valenti et al. (1995) or Rüedi et al. (1997) for the Robinson technique.

5.2 Young objects

5.2.1 The weak-line T Tauri stars V410 Tau and HDE 283572

The very low infrared excesses observed for weak line T Tauri stars suggest that the photospheres of these objects are not obscured by stellar accretion discs. This property makes them ideal candidates for studying surface inhomogeneities in active stars at very early stages of stellar evolution. In particular, magnetic field measurements are especially interesting if we want to understand better how these fully convective stars can host dynamo mechanisms, whose operation requires in principle the presence of a radiative zone to convective envelope interface layer.

Most of our observing runs being scheduled in December, little choice is left to select bright weak-line T Tauri targets visible from the AAT. Those we finally observed in 1993 Dec. are V410 Tau (K2IV) and HDE 283572 (G8IV), likely the most accessible candidates (with $m_{\rm V}$=11.0 and 8.6 respectively) known as weak-line T Tauri stars at that time. However, being northern objects, these targets are always very low on the AAT horizon (zenith distance of 60° at best), yielding a rather poor overall throughput in the blue part of the spectrum as a result of atmospheric dispersion. Both objects are only about 1 Myr old or even younger, and are known to exhibit spectroscopic and photometric rotational modulation, whose interpretation in terms of stellar surface inhomogeneities (Strassmeier et al. 1994; Joncour et al. 1994; Hatzes 1995; Joncour et al. 1994) has been proposed several times already.

Four spectra of V410 Tau were recorded on 1993 Dec. 25, 27, 28 and 29. LSD spectra yield a $v \sin i$ of 72 ± 2 km s^{-1}. The radial velocity we measure is $v_{\rm rad} = 17 \pm 2$ km s^{-1}. Dramatic profile distortions are observed in the mean unpolarised profiles of V410 Tau. Mean Stokes V signatures with a peak-to-peak relative amplitude of 0.32% are detected at a 9 σ level on Dec. 25, 28 and 29 (i.e. when the corresponding relative noise level is smaller than 0.035% rms), as shown on Fig. 4 in the particular case of the first spectrum. As these signatures are detected with a false alarm probability equal to or smaller than 10^{-10}, we can safely consider that they witness the presence of a magnetic field on V410 Tau. Note that this is the first *direct* evidence of magnetic field in a T Tauri star, after the very indirect results of Basri et al. (1992).

Eight observations of HD 283572 were recorded on 1993 Dec. 25 to 29. The $v \sin i$ and $v_{\rm rad}$ we measure for this object are respectively equal to 77 ± 2 and 15 ± 2 km s^{-1}. As noted already by Joncour et al. (1994b), the LSD Stokes I spectrum of HD 283572 constantly features a very flat-bottom line. Mean Stokes V signatures reach a total peak-to-peak amplitude of about 0.13% and 0.15% respectively (corresponding to 7 and 6 σ) on Dec. 25 and 27. The associated false alarm probability ranging between 10^{-4} and 10^{-5}, we consider that these two magnetic detections (one of which is shown on Fig. 5) are still marginal, and thus await for a definite confirmation from better quality data.

5.2.2 The classical T Tauri star SU Aur

Conversely to weak line T Tauri stars, classical T Tauri stars possess a rich circumstellar environment and often display observational evidence for both accretion discs and winds. SU Aur (G2IV) is one of the brightest and most studied members of this class. Strong emission and variability is observed in both Hα and Hβ, witnessing the presence of intense and rotationally modulated mass inflows and outflows

(Johns & Basri 1995). As most photospheric lines of SU Aur do not seem to be noticeably affected by the circumstellar environment, it is also possible to study the spatial distribution of photospheric temperature inhomogeneities and its relation with mass transfer (Petrov et al. 1996). Magnetic fields measurements are thus critically needed for this object as they would firmly establish the fact that both accretion and winds are magnetically controlled.

We observed SU Aur on 1995 Dec. 12 and 13. At an airmass of about 2.0, light losses due to moderate seeing/transparency and atmospheric dispersion are important and result in a rather low overall efficiency, with peak S/N values ranging from 80 to 110. From the unpolarised LSD profile, we estimate that $v\sin i$ and $v_{\rm rad}$ of SU Aur are respectively equal to 59 ± 2 and 15 ± 2 $\rm km\,s^{-1}$. Profile distortions in the mean Stokes I spectrum are clearly visible. No Zeeman signatures are detected down to a relative noise level of 0.04% of the continuum, implying that potential polarisation signals must be smaller than about 0.25% peak-to-peak. Note that this result is not very constraining as most detections we report in this paper are smaller than this upper limit.

5.2.3 FU Ori

FU Ori stars form a third class of cool pre-main sequence objects, whose most surprising characteristic is to present a wavelength-dependent spectral type, with a doubled absorption spectrum. Today, the most probable interpretation is that these objects are massive optically-thick accretion discs, luminous enough to outshine the central T Tauri star (Hartmann & Kenyon 1985). In this model, the spectral type wavelength dependence is explained by the radial temperature gradient in the disc, while Keplerian rotation would be responsible for the doubled absorption spectrum with wavelength-dependent line widths.

From a theoretical point of view, all physical ingredients for vigorous dynamo action are present in accretion discs. However, although some observational hints exist already, no direct evidence is available yet, magnetic fields being particularly difficult to measure in such broad spectral line objects. Being the brightest member of its class, FU Ori itself is therefore the most appropriate target for a first attempt at detecting disc magnetic fields.

A single spectrum of FU Ori was recorded on 1995 Dec. 08. The LSD unpolarised spectrum shows a broad asymmetric absorption feature, very reminiscent of double peak disk profiles. Nothing is detected in LSD Stokes V profiles down to a relative noise level of 0.033%, implying that potential Zeeman signatures must be smaller than about 0.2% peak-to-peak.

5.2.4 The Herbig Ae stars HD 100546 and HD 104237

Being the high-mass analogues of T Tauri stars, Herbig Ae/Be stars constitute another class of pre-main sequence objects. In particular, observations show that these stars possess a strong and highly structured wind. By analogy with the solar wind, one expects this wind structure (in alternating fast and slow streams) to be due to magnetic fields (Praderie et al. 1986). A direct field detection would thus represent an important progress in our global understanding of these objects; moreover, it should constitute a major MHD puzzle, as these stars are not supposed to host subphotospheric convective envelopes and should therefore not be able to trigger dynamo action.

As the first unsuccessful attempt at detecting magnetic fields in a Herbig star (namely AB Aur) involved the old, low-sensitivity ZDI analysis (Catala et al. 1993), we repeated our observations on two southern Herbig stars (HD 100546 and HD 104237) with the new multiline technique described in Sect. 4. Four spectra were recorded altogether, one for HD 100546 on 1993 Dec. 29 and three for HD 104237 on 1993 Dec. 29 and 1995 Dec. 12.

We find that the spectrum of HD 100546 (B9V) features very few photospheric lines. One of them, the strong 448.12 nm Mg II triplet, yields rough $v\sin i$ and $v_{\rm rad}$ estimates of about 65 ± 5 and 17 ± 5 $\rm km\,s^{-1}$ respectively. Its total equivalent width is only 0.020 nm (compared to 0.056 nm for the A0 Herbig star AB Aur, Böhm & Catala 1993), indicating (along with the small number of spectral lines) that the photosphere is probably significantly hotter than 10,000 K and that the B9 spectral type usually quoted for this object must be revised. One interesting observation to report in our spectrum is the presence of numerous forbidden [Fe II] lines in emission (at 477.474, 481.455, 487.449, 488.970, 490.535, 500.552, 511.163, 522.006, 526.161, 533.365 and 537.647 nm), mostly from multiplets 19F and 20F. These lines show very symmetric profiles with a full width at half maximum of about 22 $\rm km\,s^{-1}$. They are centred on 14 ± 1 $\rm km\,s^{-1}$ (just as the interstellar Na D lines), in good agreement with the stellar radial velocity found above. In particular, such forbidden line are very similar to the [O I] features measured by Böhm & Catala (1994) on a wide sample of Herbig Ae/Be stars, thus strengthening their conclusions as to the large scale geometry of the circumstellar environment in which these forbidden lines usually form. As far as magnetic fields are concerned, nothing is detected in LSD Stokes V profiles down to a relative noise level of about 0.05%, implying that potential Zeeman signatures must be smaller than about 0.3% peak-to-peak.

The spectrum of HD 104237 (A4V) features numerous spectral lines with relatively sharp profiles ($v\sin i = 12 \pm 2$ $\rm km\,s^{-1}$), implying that the star is either viewed pole-on or moderately rotating. The three mean Stokes I profiles we derived are all slightly asymmetric with a blue wing deeper than the red wing, indicating that a small wind contribution pollutes most photospheric lines. Clear radial velocity variations (with a peak-to-peak amplitude of about 1.3 $\rm km\,s^{-1}$ or 0.4 pxl around a mean radial velocity of 20 $\rm km\,s^{-1}$) are detected in LSD Stokes I spectrum at *both* observing dates (1993 Dec. 29 and 1995 Dec. 12). The corresponding periods we obtain from a sinusoidal least-squares fit to the data (38.6 ± 1 min and 36.4 ± 1 min respectively for the 1993 and 1995 sets) are both equal within the error bars. Each data set spanning no longer than 40 min (about one full cycle), the accuracy we get on radial velocity *variations* (estimated from successive exposures on sharp-line standard stars like δ Eri or the Sun) is typically 50 $\rm m\,s^{-1}$ rms (0.016 pxl), i.e. small enough to detect unambiguously a 1.3 $\rm km\,s^{-1}$ modulation. The period of the fluctuation we measure (37.5 ± 1 min in average) is much too short to be due to rotational modulation or to a secondary companion,

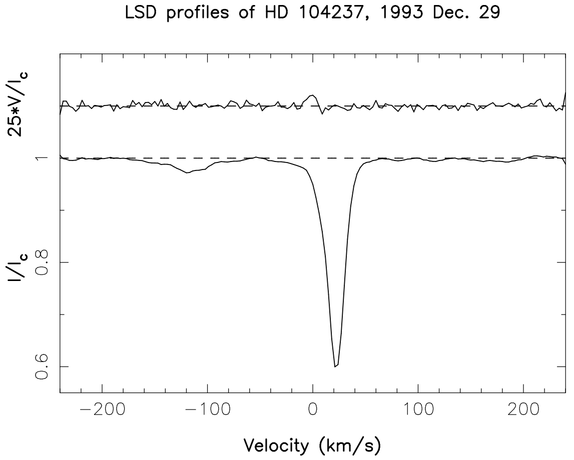

Figure 6. Same as Fig. 4 for the Herbig Ae star HD 104237 on 1993 Dec. 29

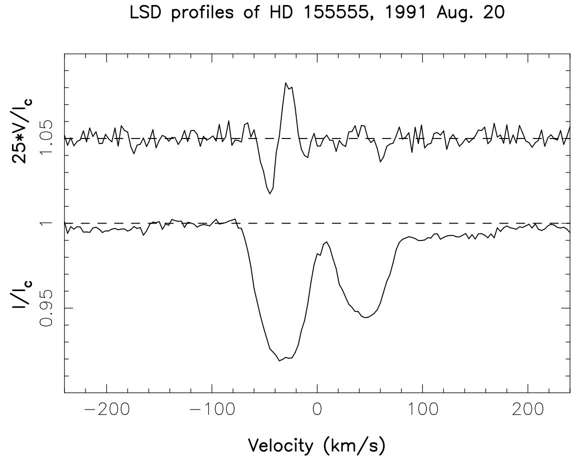

Figure 7. Same as Fig. 4 for the pre-main sequence system HD 155555 on 1991 Aug. 20. The deepest line profile of the mean Stokes I spectrum corresponds to the G5IV star, while the shallow one corresponds to the K0IV component.

and must therefore be attributed to stellar pulsations. If this interpretation is confirmed, it would imply that the corresponding pulsation is stable on timescales of at least two yr. In 1993, the high S/N values we reached enabled us to obtain a marginal magnetic detection (false alarm probability of about 10^{-5}) with a peak-to-peak relative amplitude of about 0.14% (i.e. 7 σ). As one can see on Fig. 6, this signature spatially correlates with the wind contribution in the blue wing of the mean Stokes I profile. It is interesting to note (though difficult to understand yet) that the 501.8440 nm Fe II line itself (formed at the base of the wind, i.e. slightly higher than most photospheric lines) also shows in the blue part of the profile a 7 σ Stokes V signature at a level of 0.65% peak-to-peak, i.e. about 5 times larger than the mean Zeeman signal we detect whereas this particular line is only 1.6 times more sensitive than the average. The larger spectral domain measured on 1995 Dec. 12 did not compensate for the poor weather conditions; the resulting noise level we get in the mean Stokes V spectrum (about 0.05%) hides any potential signal with an amplitude smaller than 0.3% peak-to-peak. However, if we average the two LSD Stokes V profiles obtained this night, we can just see a very marginal Zeeman signature, whose location, shape and amplitude corresponds exactly (at noise level accuracy) to that observed two years earlier. Altogether, it may indicate that the magnetic structure we marginally detected on HD 104237 is stable on timescales of several years. If confirmed, this measurement would represent the first detection of a magnetic field in a Herbig Ae/Be star.

5.2.5 *The PMS binary system HD 155555*

HD 155555 (G5IV+K0IV) is an active close binary star with an extremely high Li content (logarithmic [Li/H] abundance ratio of –8.5, Pasquini et al. 1991) suggesting that both stars have still not completed their contraction towards the main sequence. With a typical age of about 10^7 yr (Pasquini et al. 1991; Martín & Brandner 1995), this system represents an intermediate evolutionary stage between T Tauri and ZAMS objects (see next two paragraphs).

After the first unsuccessful attempt of Donati et al. (1992a), HD 155555 was observed five more times in 1991 Aug. 19, 20 and 27. The corresponding orbital phases (in Pasquini et al.'s ephemeris) are 0.485, 0.061, 0.085, 0.226 and 0.248 respectively, in very good agreement with the radial velocities we measure outside of conjunction (−33.5/45.0, −43.8/57.3, −81.8/96.9 and −82.5/97.3 $\mathrm{km\,s^{-1}}$ for the second to fifth observation and for the hot/cool components). The $v \sin i$ we measure from LSD Stokes I spectra are 34 ± 1 and 32 ± 1 $\mathrm{km\,s^{-1}}$ for the hot and cool components respectively. Mean unpolarised profiles show clear spot signatures, larger for the G5 star than for the K0 companion. Magnetic signatures are clearly detected in the first four observations (i.e. whenever S/N exceeds 350) and for both system components, with peak-to-peak relative amplitudes of 0.14% to 0.26% for the hot star, and 0.10% to 0.15% for the cool companion (see Fig. 7).

5.2.6 *The ZAMS star AB Dor*

AB Doradus (K0V) is the brightest known rapidly rotating cool dwarf with an age of only a few 10^7 yr, i.e. in the same evolutionary state as about half of the Pleiades and α Per low mass dwarfs. Its strong activity has made it the subject of numerous multiwavelength studies, from the photosphere up to the corona. In particular, we observe surface brightness inhomogeneities on AB Dor (mapped several times already, e.g. Cameron 1995), while centrifugally supported prominences trapped in closed coronal loop structures are constantly observed near the Keplerian corotation radius (Cameron & Robinson 1989a, 1989b). Magnetic measurements on AB Dor are thus particularly important in order to confirm the connection between field and prominences, and to understand the relation between the large scale field structure and the distribution of surface features.

Altogether, 64 exposures of AB Dor were recorded, on 1991 Dec. 17 and 18, and 1995 Dec. 07, 10, 11 and 12. The $v \sin i$ and $v_{\rm rad}$ we measure are respectively equal to 91 ± 2 and 31 ± 2 $\mathrm{km\,s^{-1}}$. Profile distortions in LSD Stokes I spectra are only moderate. In 1991, observations are still too noisy to allow a field detection. The new attempt of 1995 (with a much larger wavelength domain and better overall instru-

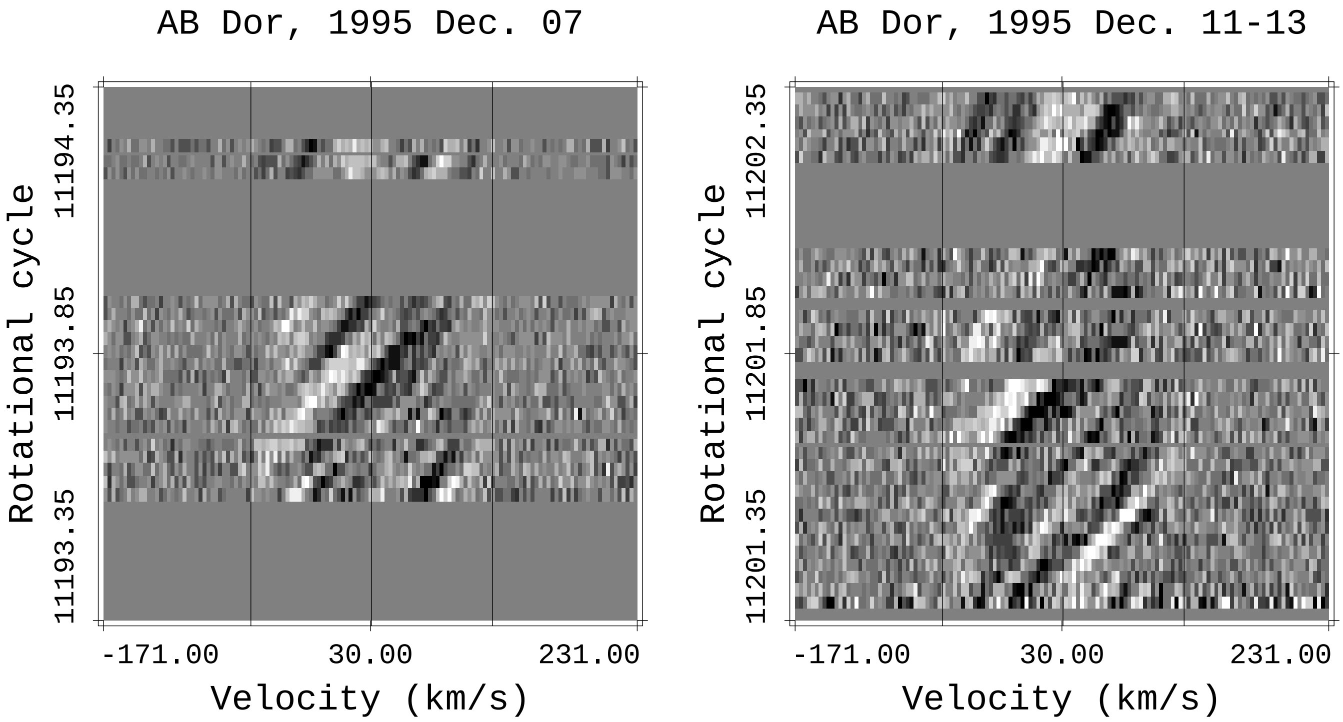

Figure 8. Stokes V dynamic spectra of AB Dor for 1995 Dec. 07 (left panel) and 1995 Dec. 11, 12 and 13 (right panel) data sets. Each line of this image corresponds to a LSD Stokes V spectrum of AB Dor coded with linear grey scales (black and white corresponding to polarisation rates of –0.06% and 0.06% respectively). To save space, data recorded on 1995 Dec. 12 and 13 (upper block of data in right panel) are plotted on the same graph as 1995 Dec. 11 data, with rotational cycle values (computed from Innis et al.'s 1988 ephemeris) offset by –1 and –3 cycles respectively. The three vertical lines in the spectra illustrate the rotational broadening and line centre (i.e. $-v\sin i{+}v_{\rm rad}$, $v_{\rm rad}$ and $v\sin i{+}v_{\rm rad}$).

mental throughput) is considerably more successful; magnetic field is detected in all but 6 Stokes V spectra recorded on 1995 Dec. 07, 11, 12 and 13, with an average 0.13% peak-to-peak LSD Zeeman signature (average noise level in mean Stokes V signatures of 0.015%). The dynamic LSD Stokes V spectra are shown on Fig. 8 for Dec. 07 (left panel) and Dec. 11 to 13 (right panel). Not only is the magnetic field detection obvious from this plot, but one can clearly see the Zeeman signatures migrating from blue to red as the star rotates. Moreover, we can note a striking similarity between both plots, further demonstrating that what we observe is indeed rotational modulation (rather than intrinsic variability). The complexity of the parent magnetic field distribution on the surface of AB Dor is already obvious from these images, on which more than ten magnetic regions can already be identified. The detailed analysis of these observations and their interpretation in terms of brightness and magnetic maps are presented in a separate paper (Donati & Cameron 1997).

5.2.7 The ZAMS star LQ Hya

LQ Hya (K0V) is another southern object, presumably as young as AB Dor given its high lithium content (logarithmic [Li/H] abundance ratio of –9.4, Vilhu et al. 1991). As in all other young active objects, surface brightness inhomogeneities are observed through rotationally modulated line profile distortions (e.g. Strassmeier et al. 1993b).

Eighteen exposures of LQ Hya were recorded, in 1991 Dec. 17 and 18, 1992 Dec. 09 to 11, 1993 Dec. 24 to 28, and 1995 Dec. 08, 12 and 13. LSD Stokes I spectra indicate $v\sin i$ and $v_{\rm rad}$ values of 27 ± 1 and 9 ± 1 km s^{-1} respectively. Large Zeeman signatures (with a relative peak-to-peak amplitude reaching 0.35% in 1991 and 1995) are detected in all but 2 exposures, i.e. whenever the resulting noise in the LSD Stokes V spectrum gets below a relative level of about 0.03% (see Table 4). Note in particular that the peak-to-peak amplitude of the LSD polarised signal reaches up to 37 times the rms noise level on 1995 Dec. 08. Within each data set, the Stokes V signature is clearly variable, most likely due to rotational modulation. The detailed interpretation of these data in terms of magnetic maps will be presented in a forthcoming paper (Donati, in preparation). However, it is already clear from the shape of the Zeeman signatures (featuring each several sign reversals) that the parent field structure is rather complex (see Fig. 9).

Being detected with a very high accuracy, the Stokes V signatures of LQ Hya can be used for the differential blue/red LSD analysis presented in Sect. 4.3. We obtain that Zeeman signatures derived with the blue submask are either equal in size (as on 1995 Dec. 08 for instance) or smaller (by up to 25%, like on 1993 Dec. 24), but *never larger* than their red equivalents. We therefore conclude that the magnetic features we detect on LQ Hya are either at photospheric temperature or cooler (by typically 500 to 1,000 K), but definitely not warmer than the surrounding photosphere.

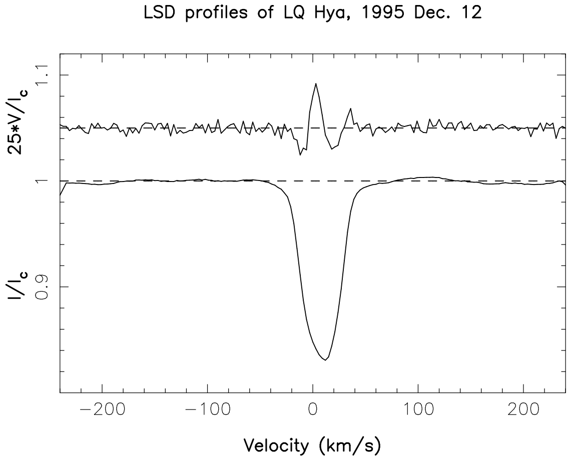

Figure 9. Same as Fig. 4 for the ZAMS star LQ Hya on 1995 Dec. 12

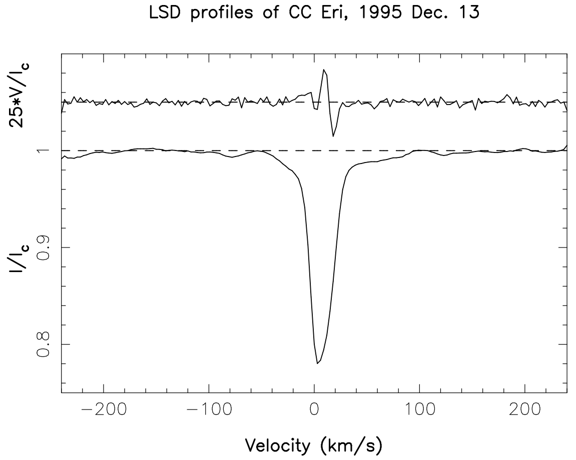

Figure 10. Same as Fig. 4 for the flare star CC Eri on 1995 Dec. 13

5.3 Main sequence objects

5.3.1 The flare star CC Eri

The single-absorption-line spectroscopic binary CC Eri (K7–9V) is an extensively studied flare star. Although a few hundred K hotter than most dMe objects, it features very similar characteristics as far as activity is concerned. Huge starspots are present at the surface of CC Eri, as witnessed by the 0.3 mag light curve rotational modulation (Strassmeier et al. 1993a). Being close to fully convective, these objects are very interesting for studies on dynamo-type magnetic field, whose production normally requires the presence of a radiative zone to convective envelope interface layer.

Three exposures of CC Eri were recorded, on 1995 Dec. 12 and 13. Given Evans' results (1959), the radial velocities we measure (43.0 and 46.1 $\mathrm{km\,s^{-1}}$ for the two Dec. 12 exposures and 7.4 $\mathrm{km\,s^{-1}}$ for Dec. 13) can uniquely be attributed to rotational phases 0.51, 0.52 and 0.16 respectively, implying that the published orbital period of CC Eri is probably slightly underestimated (by about 0.00004 d). Measuring the rotational broadening on the mean unpolarised profiles yields a $v \sin i$ of 17 ± 1 $\mathrm{km\,s^{-1}}$. A slight asymmetry in the LSD Stokes I profile is visible on Dec. 13, indicating the presence of surface features on CC Eri at the time of our observations. All three LSD Stokes V spectra feature large Zeeman signatures whose typical relative size is 0.25% peak-to-peak (see Fig. 10).

As for LQ Hya, the Zeeman signatures of CC Eri (detected at a 20 σ level or better) can be used for the blue/red differential LSD analysis of Sect. 4.3 to infer some information on the temperature contrast of the magnetic regions with respect to the surrounding photosphere. Just as in the previous case, we obtain that at both epochs, the mean Zeeman signature derived from the blue line submask is *smaller* than its red counterpart by about 20%, indicating once more that the field regions we detect are cooler than the quiet photosphere.

5.3.2 The F0 star α Hyi

Despite having very thin convective envelopes, early-type main sequence F stars like α Hyi are known to possess high temperature chromospheres indicated by the presence of very intense emission lines in their UV spectra (e.g. Simon & Landsman 1991) as well as soft X-ray emission. However, being nearly independent of $v \sin i$ (e.g. Schrijver 1993), the activity of these objects is suspected to be mostly non-magnetic, and may originate from the damping of acoustic waves generated by turbulent convection.

Four spectra of α Hyi were recorded in 1993 Dec. 27 to 29. The mean Stokes I spectrum features a purely rotational profile (with a $v \sin i$ and a v_{rad} of 158 ± 5 and 12 ± 5 $\mathrm{km\,s^{-1}}$respectively), suggesting that α Hyi features no temperature inhomogeneities on its surface. No Zeeman signatures are detected either in LSD Stokes V profiles down to a relative noise level of 0.64×10^{-4}. Both results tend to confirm that the activity of α Hyi is indeed mostly due to acoustic rather than magnetic heating.

5.4 Evolved objects

5.4.1 The RS CVn binary HR 1099

HR 1099 (K1IV+G5V) is a close double-lined spectroscopic binary, whose brightness and intense activity has made it one of the most observed stars for studying the so-called solar-stellar connection. Rotational modulation of both photometric brightness and spectral line profiles is attributed to the presence on the K1 subgiant of large migrating dark spots whose distribution has been monitored for over ten years now (Vogt et al. 1997). HR 1099 is also the first active star (other than the Sun) on which magnetic fields have been directly detected (Donati et al. 1990, 1992a) and mapped (Donati et al. 1992b) with ZDI.

We report here 57 new polarisation observations of HR 1099 altogether, recorded on 1991 Aug. 19 and 20, 1991 Dec. 16 to 18, 1992 Dec. 09 to 12, 1993 Dec. 24 to 27 and 1995 Dec. 07, 08, 09, 11, 12 and 13. The rotational broadening of the LSD Stokes I line profiles yields $v \sin i$ values of 41 ± 1 and 12 ± 1 $\mathrm{km\,s^{-1}}$ for the K1 and G5 components respectively. Large starspot signatures almost continuously distort the mean unpolarised line profiles of the K1 subgiant. All but one LSD Stokes V spectra show clear evidence of magnetic field on the primary K1 subgiant of HR 1099 (at an accuracy of up to 50 σ on 1992 Dec. 11), with Zeeman

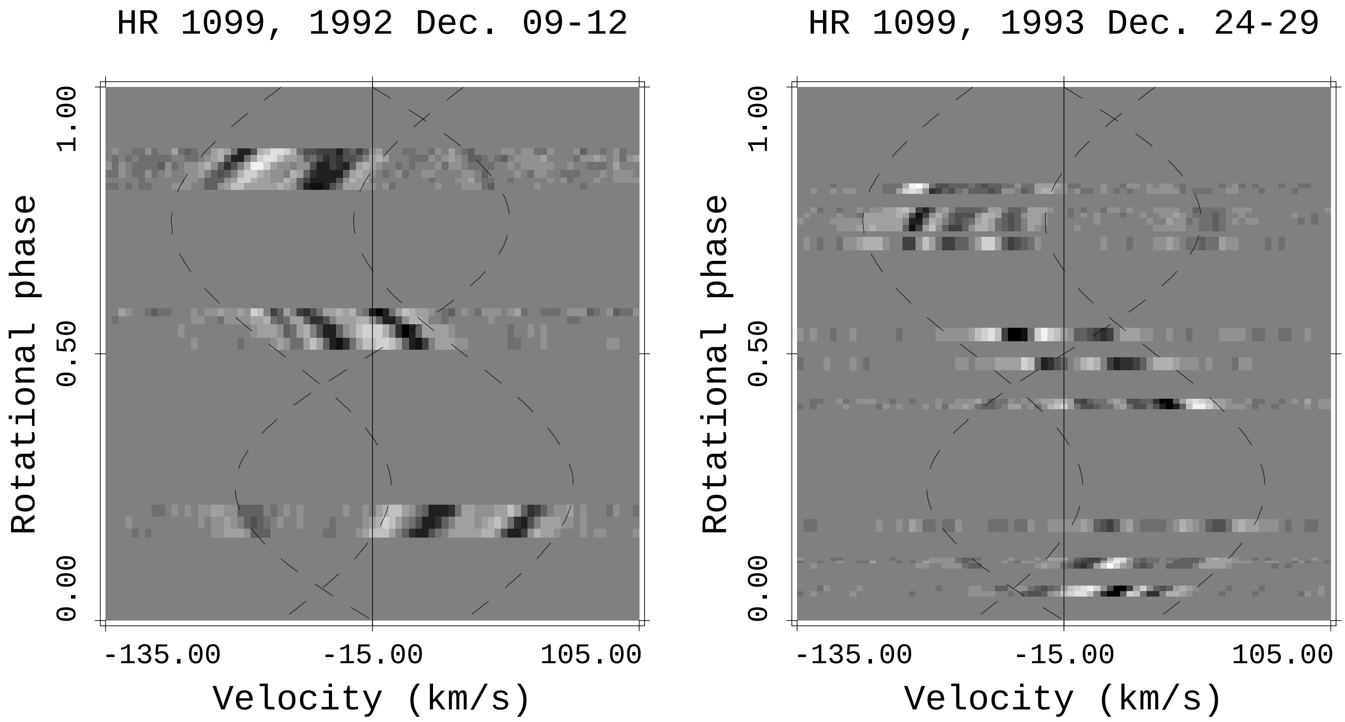

Figure 11. Stokes V dynamic spectra of HR 1099 in 1992 Dec. (left panel) and 1993 Dec. (right panel). Each line of this image corresponds to a LSD Stokes V spectrum of HR 1099 coded with linear grey scales (black and white corresponding to polarisation rates of –0.1% and 0.1% respectively). The full vertical line notes the systemic velocity, the two parallel dashed sinusoids delimit the velocity range of the K1 subgiant as a function of rotational phase while the third dashed sinusoid depicts the orbit of the G5 component.

signatures whose total relative amplitude fluctuates between 0.1 and 0.25% peak-to-peak as the star rotates (see Fig. 11 for 1992 Dec. and 1993 Dec. data sets). An important point is that polarisation spectra recorded exactly one cycle apart (e.g. on 1992 Dec. 09 and 12 at orbital phases 0.85 to 0.87, depicted in the top data block of Fig. 11, left panel) are in perfect mutual agreement, suggesting again that what we observe is indeed rotational modulation. Moreover, although phase coverage is much poorer than for AB Dor, one can find some hints that the Zeeman signatures migrate from blue to red within the line profiles of the cool system component. Note also that the shape of Zeeman signatures (featuring several sign reversals throughout the line profile) makes it clear that the parent field structure is fairly complex. Another interesting result is that definite Zeeman signatures are observed in conjunction with the secondary component as well, the most obvious ones (observed on 1992 Dec. 10 at orbital phases 0.15 to 0.20, Fig. 11, left panel) reaching a total amplitude of 0.05% peak to peak (i.e. about 15 to 20 times the rms noise level). A careful look at Fig. 11 reveals that the secondary Zeeman signature is indeed visible most of the time, but remains much smaller than that of the primary star with typical relative amplitudes of 0.02% to 0.03%.

The blue/red differential LSD analysis outlined in Sect. 4.3 indicates again than Stokes V signatures derived with the blue submask are systematically 20% to 40% *smaller* than those obtained with the red submask (see Fig. 12). We interpret this point as further evidence that the magnetic regions we detect on the K1 component of HR 1099 are cooler (by typically 500 to 1000 K) than the surround-

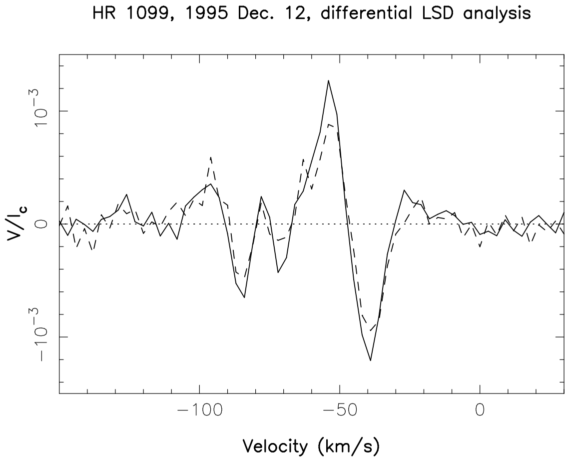

Figure 12. LSD Stokes V signatures of HR 1099 on 1995 Dec. 12, using the red (full line) and blue (dashed line) spectral submasks (see text)

ing photosphere. The detailed interpretation of these data in terms of magnetic mapping will be published in a separate paper (Donati 1997).

5.4.2 *The short period RS CVn binaries EI Eri, SZ Psc, TY Pyx and CF Tuc*

All four systems are very active objects and are known to feature surface brightness inhomogeneities. Two of them (EI Eri and SZ Psc) were already observed with the older

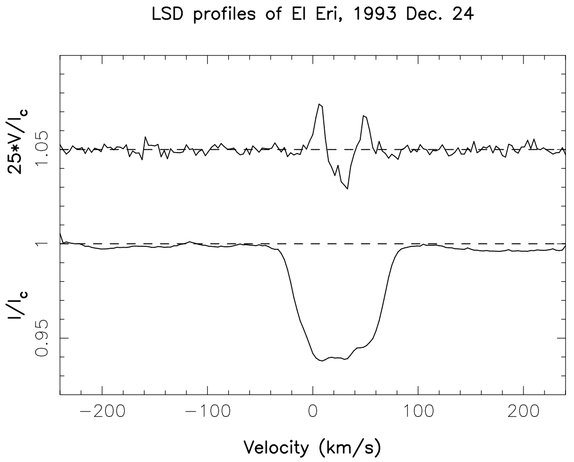

Figure 13. Same as Fig. 4 for the RS CVn system EI Eri on 1993 Dec. 24

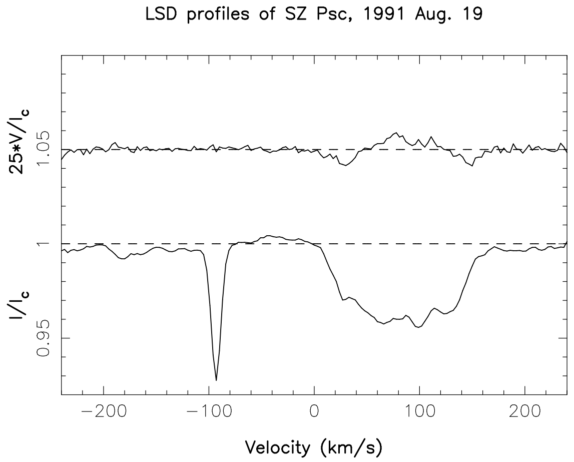

Figure 14. Same as Fig. 4 for the RS CVn system SZ Psc on 1991 Aug. 19. The broad (resp. shallow) line profile in the LSD Stokes *I* spectrum corresponds to the K1IV (resp. F8IV) system component.

version of ZDI, but no evidence of magnetic fields was obtained (Donati et al. 1992a). Both were observed again with the improved ZDI instrumental setup and analysis.

Two exposures of EI Eri (G5IV) were recorded on 1993 Dec. 24 and 26, i.e. very slightly more than one rotation cycle apart, at rotational phases 0.406 and 0.415 respectively (using Strassmeier's ephemeris 1990). The mean unpolarised profile of EI Eri shows clear rotational broadening (whose measurement yields $v \sin i = 51 \pm 1$ km s^{-1}) and obvious starspot signatures. Note that the radial velocities we measure for EI Eri at both epochs (24.5 ± 1 and 23.5 ± 1 km s^{-1} respectively) are in strong disagreement with Strassmeier's ephemeris (1990), which therefore need to be revised as already suggested by Gunn et al. (1996) from completely independent data. As one can see from Fig. 13, LSD Stokes *V* spectra of EI Eri feature strong Zeeman signatures (whose relative amplitude reaches 0.2% peak-to-peak). Both Stokes *V* profiles (recorded almost exactly one cycle apart) show a perfect mutual agreement (down to photon noise level), still reinforcing the idea that they are rotationally modulated magnetic signatures of a given field topology (rather than intrinsic variability). Partial blue and red LSD Stokes *V* profiles are both equal at photon noise accuracy, implying that the magnetic regions we detect are roughly at the same temperature as the surrounding photosphere. Four exposures of SZ Psc (F8IV+K1IV) were collected in 1991 Aug. 19 and 20. The mean Stokes *I* profiles of the cool primary system component show a rotational broadening corresponding to $v \sin i = 71 \pm 2$ km s^{-1}, with obvious starspot signatures. The absorption profile of the secondary F8 subgiant is very narrow, with a full width at half maximum of 11 km s^{-1}, in good agreement with the published total line broadening of 9 km s^{-1} if we take into account the spectral resolution of our observations (6 km s^{-1} in 1991 Aug., see Table 1). The radial velocities we measure for the hot/cool system components are equal to −90.4/77.5, −93.2/79.2, −95.3/80.5 and −15.8/22.0 km s^{-1} for each exposure respectively, with typical error bars of 1/2 km s^{-1}. Given the period change of SZ Psc (Kalimeris et al. 1995), we used the contemporaneous ephemeris of Eaton & Henry (1997) to determine the orbital phases corresponding to our observations. The values we find (0.182, 0.195, 0.208 and 0.460 respectively)

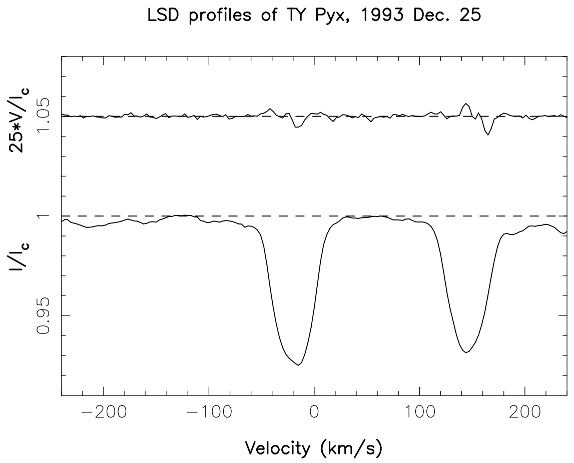

Figure 15. Same as Fig. 4 for the RS CVn system TY Pyx on 1993 Dec. 25. The deepest line profile corresponds to the more massive component.

are in good agreement with the radial velocities we report, if we increase them all by about 5 km s^{-1}. The origin of this global shift is still unclear, and cannot be attributed to some calibration errors in our data, as other spectra (those of 42 Cap, the Sun and HD 155555 in particular) do not show the same problem. Zeeman signatures with an amplitude of 0.09% peak-to-peak are detected on all three Aug. 19 observations. Being in good mutual agreement at noise level accuracy, the three Stokes *V* signatures are averaged together to make the resulting magnetic signal (detected at a 15 σ level) even more obvious (see Fig. 14).

Seven exposures of TY Pyx (G5IV+G5IV) were obtained on 1993 Dec. 24 to 28. The corresponding orbital phases are 0.527, 0.833, 0.843, 0.145, 0.160, 0.455 and 0.771 according to the ephemeris of Andersen et al. (1981), which agrees extremely well with the radial velocities we measure for the hot/cool components (–81.4/45.0, 145.7/–20.2, 142.6/–17.1, –13.8/140.1, –19.0/145.3, 37.4/87.8 and 159.1/–32.9 km s^{-1} for each exposure respectively, with typical error bars of less than 1 km s^{-1}). The rotational broad-

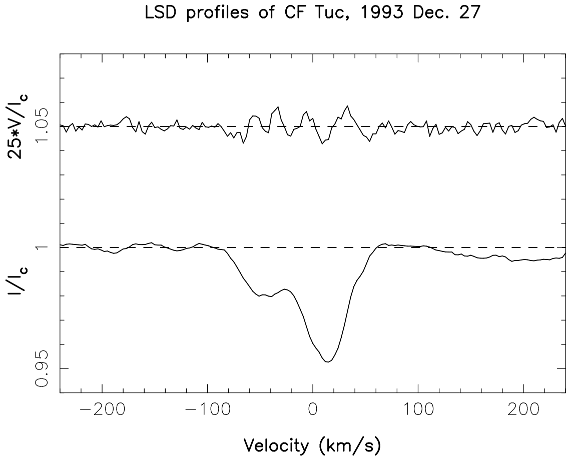

Figure 16. Same as Fig. 4 for the RS CVn system CF Tuc on 1993 Dec. 27. The system is observed near the second conjunction (hot star in front) as one can see from the overlapping line profiles.

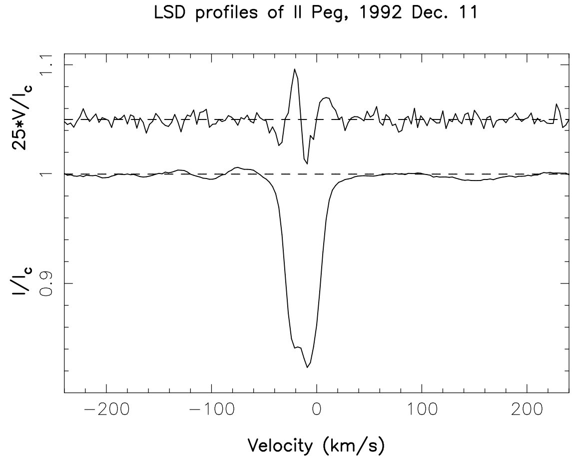

Figure 17. Same as Fig. 4 for the RS CVn system II Peg on 1992 Dec. 11

ening of mean Stokes I profiles yields $v\sin i$ values of 27 ± 1 and 28 ± 1 km s^{-1} for the hot and cool system components respectively. The magnetic field of TY Pyx is clearly detected on both components in all spectra (with small Zeeman signatures of 0.07% peak-to-peak amplitude, see Fig. 15), except on Dec. 26 when the mean photon noise in LSD Stokes V profile (equal to 0.015%) remains too large to allow a clear detection of such small magnetic signals.

Three exposures of CF Tuc (G0V+K4IV) were collected on 1993 Dec. 27 to 29. The radial velocities we measure for the hot/cool components are 10.9/–12.5, 70.1/–68.2 and –100.2/87.6 km s^{-1} for each epoch respectively, with typical error bars of 1/2 km s^{-1}. The orbital phases we derive from Kürster's (1996) new ephemeris (equal to 0.540, 0.896 and 0.253) are systematically too large (by about 2.5% of an orbital cycle) for the radial velocities we measure, suggesting that the present orbital period is slightly underestimated. Rotational broadening of mean Stokes I profiles indicate $v\sin i$ values of 25 ± 1 and 70 ± 2 km s^{-1} for the hot and cool system components respectively. A clear Zeeman signature (reaching a peak-to-peak amplitude of 0.07% and featuring as many as eight successive sign reversals) is detected at a 8 σ level close to the second system conjunction (orbital phase 0.540, see Fig. 16), thus providing direct evidence that the K4 component (at least) hosts a complex photospheric magnetic field.

5.4.3 The long period RS CVn binaries II Peg, IL Hya, IM Peg and 42 Cap

To study in more detail the influence of rotation on the magnetic field structure, it is also important to observe objects with longer rotational periods. In that respect, RS CVn systems II Peg, IL Hya and IM Peg are particularly interesting, their $v\sin i$ remaining above the 20 km s^{-1} threshold below which magnetic spots of opposite polarities tend to cancel mutually their signatures. For the same reason, 42 Cap (whose $v\sin i$ equals 5.5 km s^{-1} according to Strassmeier et al. 1993a) is probably not as good a candidate.

Two exposures of II Peg (K2IV) were recorded on 1992 Dec. 10 and 11. We estimate the radial velocity of II Peg to be -46.5 ± 1 and -13.2 ± 1 km s^{-1} for each observation respectively, and measure a rotational broadening of 22 ± 1 km s^{-1}. The orbital phases we obtain for each epoch (0.853 and 0.002 in Vogt's ephemeris 1981) are both underestimated (by about 1.5% of an orbital cycle) given the radial velocities we measure, suggesting that the orbital period of II Peg is actually slightly smaller than Vogt's estimate. As far as magnetic field are concerned, both spectra show clear evidence of large Zeeman signatures (with a peak-to-peak relative amplitude of about 0.34%, see Fig. 17), thus confirming the earlier detection of Donati et al. (1992b). The blue/red differential LSD analysis indicates once more that the magnetic regions we detect on II Peg are at the same temperature or slightly cooler than its surrounding photosphere.

The binary system IL Hya (K2III) was observed twice in 1993 Dec. 27 and 28. The corresponding radial velocities we measure for the K2 giant are equal to 3.2 and 21.3 km s^{-1} respectively. As one can see on Fig. 18, mean Stokes I profiles clearly show the presence of a secondary spectrum (at radial velocities of –26.4 and –57.3 km s^{-1} for each epoch respectively), whose detection now locates IL Hya in the class of double-line spectroscopic binaries. From these elements, we can derive the stellar fundamental parameters for each system component. First of all, our measurements (along with the published system orbital elements, Strassmeier 1993a) imply that the radial velocity amplitude of the small companion is equal to 66.8 ± 0.8 km s^{-1}, and thus that the secondary to primary star mass ratio is 0.63 ± 0.02. Given an arbitrary system inclination, we can then derive a value for both the primary star radius (from the line rotational broadening of 25 ± 1 km s^{-1} we measure and the fact that the system is synchronised) and mass (from the system orbital period and the radial velocity amplitudes of both components), which in turn yields another radius estimate (given the published $B-V$ colour index of IL Hya corresponding to an effective temperature of 4750 K) from the new evolutionary models of Schaller et al. (1992). It is only for a short range of system inclinations ($i=59\pm4°$) that these two radius estimates can be matched within the error bars, yielding final stellar parameters of 1.7 ± 0.2 $M_\odot$ and 7.5 ± 0.4 $R_\odot$ for the primary star. The corresponding

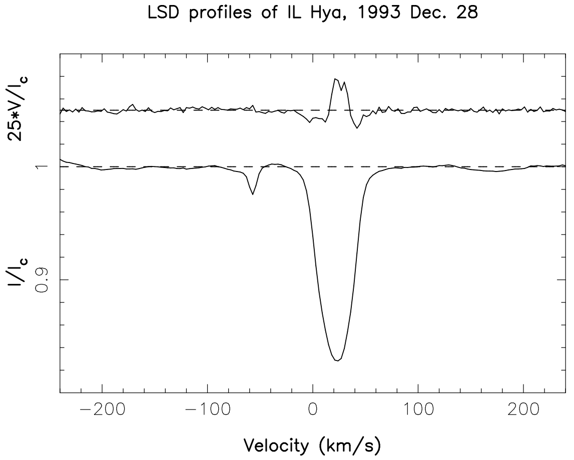

Figure 18. Same as Fig. 4 for the RS CVn system IL Hya on 1993 Dec. 28. Note the detection in the mean Stokes I profile of the secondary system component (at a radial velocity of –57.3 $\mathrm{km\,s^{-1}}$).

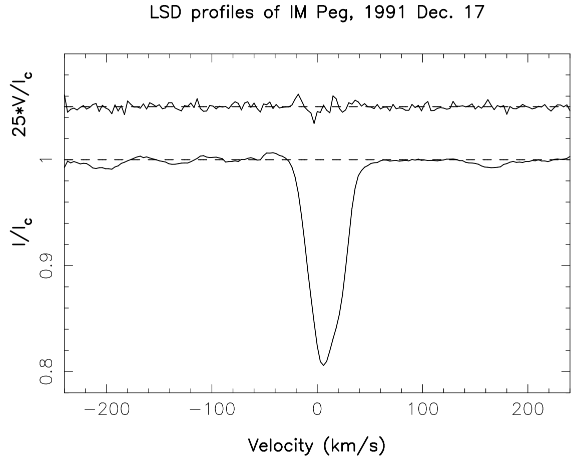

Figure 19. Same as Fig. 4 for the RS CVn system IM Peg on 1991 Dec. 17

secondary companion (given the inferred mass ratio and age of primary star) must weigh $1.1 \pm 0.1\ M_{\odot}$, with a radius and temperature of $1.0 \pm 0.2\ R_{\odot}$ and 5900 ± 250 K respectively. Going back to our data, we can check that a blue/red LSD differential analysis (with a K1 mask) applied to Stokes I spectra yields a mean secondary line profile *deeper* in the blue than in the red, thus confirming that the companion is hotter than the primary star. Moreover, comparing, in our spectra of IL Hya, the depth of the companion mean line with that of a LSD Stokes I profile of the Sun yields an approximate luminosity ratio of 23 between the cool and hot star, in good agreement with the predicted value of 24 resulting from the stellar fundamental parameters we obtained. Finally, comparing again with a LSD Stokes I profile of the Sun, the mean line profile of the secondary star of IL Hya shows a broadening excess of about 4.4 $\mathrm{km\,s^{-1}}$ rms, roughly compatible with the $v \sin i$ the secondary star would have (3.6 $\mathrm{km\,s^{-1}}$) if its rotation is synchronised with the orbit. As illustrated on Fig. 18, Zeeman signatures (with a peak-to-peak relative amplitude of 0.2%) are unambiguously detected at both epochs on the K2 giant. A differential blue/red LSD analysis indicates once more that the magnetic regions we detect are roughly as warm as or slightly cooler than the surrounding photosphere.

The single-line spectroscopic binary IM Peg (K2III) has the longest period of our sample (24.65 d) and was observed only once on 1991 Dec. 17. Mean Stokes I indicate a rotational broadening and a radial velocity of 25 ± 1 and 8.3 ± 1 $\mathrm{km\,s^{-1}}$respectively. As illustrated on Fig. 19, a clear Zeeman signature (with a peak-to-peak relative amplitude of 0.12%) is detected.

Finally, two exposures of 42 Cap (G2IV) were recorded on 1991 Aug. 19 and 20 respectively, at orbital phases 0.14 and 0.22. As for IL Hya, the two system components are clearly visible in the mean Stokes I profiles, with radial velocities of 13.9/–22.1 and 17.8/–28.3 $\mathrm{km\,s^{-1}}$ for the primary/secondary star at both epochs respectively (in good agreement with the orbital phases quoted above). Although the detection of the secondary star is already reported in the literature (Strassmeier et al. 1993a), fundamental stellar parameters of both components are not available. As for IL Hya, we first derive from our measurements (along with the published system orbital parameters) a secondary to primary star mass ratio is 0.72 ± 0.01. For any arbitrary system inclination, we can again derive a value for both primary star mass (from the system orbital period and the radial velocity amplitudes of both components) and radius (from an estimated effective temperature of 5750 K together with Schaller et al.'s models, 1992). As we do not know a priori if the system is synchronised, we have to use now the luminosity ratio between components, estimated to be 6.5 ± 0.3 from the LSD Stokes I profiles. Once more, only a small range of inclination angles ($i = 24.5 \pm 1.5°$) can yield stellar fundamental parameters that match this luminosity ratio within the error bars. We find that the mass and radius of the primary star are equal to $1.5 \pm 0.1\ M_{\odot}$ and $3.0 \pm 0.3\ R_{\odot}$, and that the mass, radius and temperature of the companion are $1.1 \pm 0.1\ M_{\odot}$, $1.1 \pm 0.2\ R_{\odot}$ and 5950 ± 250 K. Once again, we can cross-check through differential LSD of our Stokes I spectra that both components have indeed similar temperatures. We can also note that the published $v \sin i$ of the G2 subgiant (5.5 ± 1.0 $\mathrm{km\,s^{-1}}$, Strassmeier et al. 1993a, compatible with the 6.7 ± 1.0 $\mathrm{km\,s^{-1}}$ rms broadening excess with respect to solar lines measured in the mean Stokes I profiles) suggests that the rotation of the primary star is almost synchronised with the orbit (requiring $v \sin i = 4.7 \pm 0.5$ $\mathrm{km\,s^{-1}}$ according to the stellar parameters derived above). Given its long orbital period, 42 Cap has probably undergone synchronisation only very recently and is on its way to circularisation (a stage that IL Hya has reached already), in good agreement with the new tidal friction calculations of Zahn & Bouchet (1989). On Aug. 19, we detect a marginal signature (false alarm probability of 10^{-4}), with a relative peak-to-peak amplitude of 0.04%. As this is about as large as spurious polarisation signals can be in such sharp-line stars (due to internal spectrograph stability problems for instance, see Sect. 5.1.1), we therefore do not consider this detection as reliable.

5.4.4 The FK Com star YY Men

Observations tell us that FK Com stars are very active single low-mass giants whose rapid rotation constitute an astro-

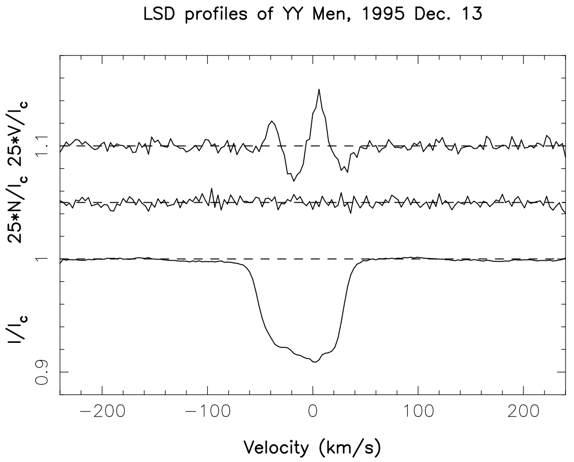

Figure 20. Same as Fig. 4 for the FK Com star YY Men on 1995 Dec. 13. The null polarisation spectrum N is displayed between the Stokes V (upper graph) and Stokes I (lower graph) profiles.

physical puzzle, most similar stars ending up on the red giant branch as slow rotators after several episodes of strong rotational braking. The most common explanation is that these objects result from the progressive merging of close/contact binary stars. One of them, YY Men (K1III), is known to be one of the most active stars in the sky (e.g. Cutispoto et al. 1992) and to feature large scale surface brightness inhomogeneities (e.g. Piskunov et al. 1990), and is thus a particularly good candidate for stellar photospheric field studies.

We observed YY Men three times, on 1995 Dec. 08, 12 and 13. Mean Stokes I profiles show very large starspot signatures. Our estimates for the rotational broadening and radial velocity are equal to 45 ± 1 and -10.9 ± 1 km s^{-1}. As one can see from Fig. 20, this object features the strongest Zeeman signatures of our sample, with peak-to-peak relative amplitudes ranging from 0.17% (on 1995 Dec. 12) up to 0.35% (on 1995 Dec. 13). Note that we also show on Fig. 20 the null polarisation spectrum N corresponding to the 1995 Dec. 13 exposure sequence on YY Men. The total absence of any detectable signal (at noise level accuracy) demonstrates in particular that the Stokes V signatures we detect for YY Men indeed correspond to true circular polarisation (see Sects. 3.4) and illustrates in general the kind of N spectra we obtain on all other programme objects (as long as their true polarisation signal is not too rapidly time variable within the exposure sequence, see Sect. 5.1.1). A differential blue/red LSD analysis indicate that these Zeeman signatures are about 20% smaller in the blue than in the red, suggesting once more that the magnetic regions we detect are cooler than the surrounding photosphere.

6 SUMMARY AND CONCLUSIONS

We present in this paper the first results of 5 yr of AAT spectropolarimetric observations of active stars, using a Cassegrain visitor polarimeter coupled to the UCL Echelle Spectrograph through a fibre link. Two hundred and twenty nine polarisation spectra were altogether recorded, on a sample of 28 objects (including 21 programme stars and 7 calibration standards), with the aim of detecting and mapping magnetic fields at the surface of rapidly rotating active stars (Zeeman-Doppler imaging or ZDI).

An automatic reduction software package called ESpRIT (inspired from optimal extraction techniques) was developed for that particular purpose and is found to behave very well, especially in tricky conditions where other codes usually fail (e.g. when the spectrograph slit projection onto the CCD is not aligned with either chip lines or columns).

We also introduce a new technique to extract very small polarisation signatures dubbed "Least-Squares Deconvolution" (LSD), which shares some similarities with other cross-correlation techniques in the sense that it uses simultaneously the information from most available spectral lines in the recorded wavelength domain. For cool stars whose spectrum features numerous spectral lines, the efficiency increase is huge, reaching 7.5 mag in flux in the particular case of a K1 star with respect to a single average line technique, or 4.5 mag compared to the old three-line analysis of Donati et al. (1992a). We also demonstrate that this technique can be successfully applied to unpolarised spectra and yield comparable sensitivity improvements for other similar studies such as mapping of stellar surface inhomogeneities (Donati & Cameron 1997).

The instrumental setup, observing procedure, extraction package and "Least-Squares Deconvolution" were all carefully tested. We demonstrate in particular that this global configuration allows to measure reliably polarisation signatures with relative peak-to-peak amplitudes as low as 0.05% on the rapidly rotating objects we are interested in. When tested on magnetic Ap stars, the longitudinal field estimates we obtain are in very good agreement with previously published values, implying that the magnetic fluxes we measure with the improved multiline version of ZDI are not subject to systematic over or underestimation problems such as those reported recently for another completely independent stellar magnetic field measurement technique (Rüedi et al. 1997).

Among the 21 object sample we concentrated on, magnetic fields are unambiguously detected on 14, namely the weak-line T Tauri star V410 Tau, the pre-main sequence binary HD 155555, the ZAMS stars AB Dor and LQ Hya, the flare main sequence binary CC Eri, the RS CVn systems HR 1099, EI Eri, TY Pyx, CF Tuc, SZ Psc, II Peg, IM Peg and IL Hya, and finally the FK Com star YY Men. Marginal detections are also obtained for the weak-line T Tauri star HD 283572 and the Herbig Ae star HD 104237. Except for HR 1099 and II Peg, our detections represent the first *direct* evidence that these objects host a photospheric magnetic field.

Zeeman-Doppler imaging is found to be very efficient at detecting the complex magnetic structures of active stars. Magnetic fields are indeed detected on all RS CVn systems of our sample, except on 42 Cap whose slow rotational velocity makes it a very poor candidate. All cool young stars also show clear or marginal evidence of magnetic field, except SU Aur for which poor weather conditions did not allow us to record sufficiently good quality spectra. The other targets on which no field is detected are either hot active stars (Herbig Ae star HD 100546 and early-type active star α Hyi) or accretion discs (FU Ori) whose magnetic origin of the activity is still uncertain (HD 100546 and FU Ori) or even very unlikely (α Hyi). If the marginal detection we obtained on the Herbig Ae star HD 104237 is real, it at least explains why we do not detect any field on HD 100546, the photon noise limit reached for this star being about three times larger than for HD 104237.

The Zeeman signatures we detect on cool stars almost always feature a very complex shape with many successive sign reversals throughout the line profile (as many as eight in the particular case of CF Tuc), providing further evidence that the field structure of such active stars is rather complicated, with many separate magnetic regions of opposite polarities and/or different field orientations.

For all cool stars on which Zeeman detections are recorded with sufficient accuracy (namely LQ Hya, CC Eri, HR 1099, II Peg, IL Hya and YY Men), differential Least-Squares Deconvolution from both blue and red part of the spectral domain indicates that the the Zeeman signal at blue wavelengths is either similar in size, or smaller (by up to 40%), but never larger than its red equivalent. It clearly implies that the magnetic regions we detect are often 500 to 1,000 K cooler, sometimes at the same temperature, but in any case never warmer than the surrounding photosphere. Note that it does not mean that magnetic regions cannot be more than 1000 K cooler than the photosphere, nor that we do not detect the Stokes V signatures of these cooler regions. Having selected for each of the six stars mentioned above the largest detected polarisation signals (i.e. those measured with the highest accuracy), we therefore only investigated the hottest magnetic regions with this analysis, the overall size of Stokes V signatures depending indeed strongly on the local photospheric brightness. Zeeman signatures from cooler magnetic regions are likely also present in some of the LSD Stokes V profiles we obtain; if their amplitude is quite small (e.g. about 4 times smaller than those from the warmest detected magnetic regions for an additional 750 K temperature deficit with respect to these hotter features), they should still be detectable whenever polarisation signals from these warmer regions are measured with a very high accuracy (typically 30 to 50 σ as in Sect. 5.4.1). It is nontheless true that even if detectable in principle, Zeeman signatures from cooler regions will be very hard to identify unambiguously with the naked eye (i.e. without the help of a stellar surface imaging package) if amongst those from hotter magnetic regions. We can also conclude that the presence on the stellar surface of magnetic regions *warmer* than the surrounding photosphere (whose existence was suggested a few years ago by Donati et al. 1990, 1992b) must be a very rare occurrence (if not simply an artifact).

This first direct detection of a magnetic field in a supposedly fully convective star (the T Tauri object V410 Tau) represents an interesting challenge for either dynamo theories (which usually quote the presence of an interface layer between the inner radiative zone and outer convective envelope as an essential ingredient) or evolutionary models of pre-main sequence stars (predicting that such objects should possess no inner radiative zone). Explaining the presence of a dynamo-type magnetic field on more massive pre-main sequence stars such as HD 104237 (supposedly fully radiative according to the recent evolutionary models of Palla & Stahler 1993) is even more challenging in the framework of dynamo theories, but may find a qualitative answer in the recent suggestion of Vigneron et al. (1990) and Lignières et al. (1996) that subphotospheric turbulent motions (and hopefully magnetic fields) could appear and propagate towards the radiative stellar interior as a consequence of the strong rotational braking torque the wind imposes to the stellar photosphere.

Unfortunately, our attempts at correlating the amplitude of the Zeeman signatures we detect for rapidly rotating cool stars with the stellar fundamental parameters of interest for dynamo theories (e.g. rotation rate, spectral type, $v \sin i$) are mostly inconclusive, apart for the trivial result that Zeeman signatures get weaker for increasing $v \sin i$ (just as spectral lines get shallower at higher stellar rotational velocities). We can indeed observe vastly different amplitudes of Zeeman signatures on stars that are altogether very similar in both spectral type and $v \sin i$, like for instance II Peg and the K0IV star of HD 155555 (featuring magnetic signals with a peak-to-peak relative amplitude of 0.35% and 0.12% respectively). The most likely explanation for this null result is that the size of magnetic polarisation signals depends strongly on several variables other than just the average magnetic flux (and in particular on the local photospheric brightness, or on the typical size of individual unipolar magnetic regions which in turn may depend on the evolutionary phase within an activity cycle), rendering any single variable correlation analysis globally unsuccessful.

The conclusion is thus that such correlations will only be possible when full reconstructions of photospheric field structures are available for a large sample of objects. These images should indeed allow us to access local quantities such as magnetic flux for instance that could then be correlated with fundamental stellar parameters. The data presented herein should already allow us to do so for at least three targets (namely AB Dor, HR 1099 and LQ Hya), at different epochs. The corresponding maps are or will be published in separate papers (Donati & Cameron 1997; Donati 1997). Another advantage of this approach is that we can also access the magnetic field orientation and polarity (Donati & Brown 1997) together with its progression in time (as the star evolves along its activity cycle) and compare the results with the field topologies predicted by various dynamo models (e.g. overshoot layer vs. distributed dynamo, Brandenburg et al. 1994). Our aim is thus to continue this study and obtain rich enough data sets on a few well selected objects all the way from the pre-main sequence stage up to the red giant branch to test existing dynamo models and suggest new theoretical possibilities.

ACKNOWLEDGEMENTS

We thank S.F. Brown, J.D. Thatcher, B.J. O'Mara and J. Li for their participation to data collection, and O. Durand for his active involvement and technical assistance during the construction, testing and use of the polarimeter at the AAT. We also thank the AAT staff for his very valuable help throughout most observing nights. Finally, an anonymous referee is acknowledged for suggesting several improvements to the paper. This work was based on data collected with the UCL Echelle spectrograph at the AAT

REFERENCES

Allington-Smith J.R., Breare J.M., Carrasco B.E., et al., MNRAS 238, 603

Andersen J., Clausen J.V., Nordstrom B., Reipurth B., 1981, A&A 101, 7

Babel J., North P., 1997, A&A (in press)

Basri G., Marcy G.W., Valenti J.A., 1992, ApJ, 390, 622

Basri G., Marcy G.W., 1994, ApJ, 431, 844

Bohlender D.A., Landstreet J.D., Thompson I.B., 1993, A&A 269, 355

Bohlender D.A., 1988, PhD thesis, University of Western Ontario

Böhm T., Catala C., 1994, A&A 290, 167

Böhm T., Catala C., 1993, A&AS 101, 629

Brandenburg A., Saar S.H., Moss D., Tuominen I., 1994, in: Caillault J.-P. (eds.), 8th Cambridge Workshop on "Cool Stars, Stellar Systems and the Sun". PASP Conf. Series 64, p. 357

Bonsack W.K., 1976, ApJ 209, 160

Borra E.F., Edwards G., Mayor M., 1984, ApJ 284, 211

Brown D.N., Landstreet J.D., 1981, ApJ 246, 899

Brown S.F., Donati J.-F., Rees D.E., Semel M., 1991, A&A 250, 463

Cameron A.C., 1995, MNRAS 275, 534

Cameron A.C., Robinson R.D., 1989a, MNRAS 236, 57

Cameron A.C., Robinson R.D., 1989b, MNRAS 238, 657

Carter B.D., Brown S.F., Donati J.-F., Rees D.E., Semel M., 1996, PASA 13, 150

Catala C., Böhm T., Donati J.-F., Semel M., 1993, A&A 278, 187

Cutispoto G., Pagano I., Rodonò M., 1992, A&A 263, L3

Donati J.-F., Brown S.F., 1997, A&A (in press)

Donati J.-F., Brown S.F., Semel M., Rees D.E., et al., 1992b, A&A 265, 682

Donati J.-F., Cameron A.C., 1997, MNRAS (in press)

Donati J.-F., Semel M., Rees D.E., 1992a, A&A 265, 669

Donati J.-F., Semel M., Rees D.E., Taylor K., Robinson R.D., 1990, A&A 232, L1

Eaton J.A., Henry G.W., 1997, PASP (in press)

Evans D.S., 1959, MNRAS 119, 526

Gunn A.G., Hall J.C., Lockwood G.W., Doyle J.G., 1996, A&A 305, 146

Hartmann L., Kenyon S.J., 1985, ApJ 299, 462

Hatzes A., 1995, ApJ 451, 784

Horne K., 1986, PASP 98, 609

Innis J.L., Thomson K., Coates D.W., Lloyd Evans T., 1988, MNRAS 235, 1411

Johns C.M., Basri G., 1995, ApJ 449, 341

Joncour I., Bertout C., Ménard F., 1994, A&A 285, L25

Joncour I., Bertout C., Bouvier J., 1994, A&A 291, L19

Kalimeris A., Mitrou C.K., Doyle J.G., Antonopoulou E., Rovithis-Livaniou H., 1995, A&A 293, 371

Kürster M., 1996, in: Strassmeier K.G., Linsky J.L. (eds.), IAU Symp. 176, "Stellar Surface Structure". Kluwer Academic Publishers, Dordrecht, p. 477

Kurucz R.L., 1993, CDROM # 13 (ATLAS9 atmospheric models) and # 18 (ATLAS9 and SYNTHE routines, spectral line database)

Landstreet J.D., 1988, ApJ 326, 967

Lignières F., Catala C., Mangeney A., 1996, A&A 314, 465

Marsh T.R., 1989, PASP 101, 1032

Martín E.L., Brandner W., 1995, A&A 294, 744

Mathys G., 1990, A&A 232, 151

Mathys G., 1991, A&AS 89, 121

Mathys G., Hubrig S., 1997, A&AS 124, 475

Mathys G., Hubrig S., Landstreet J.D., Lanz T., Manfroid J., 1997, A&AS 123, 353

Mayor M., 1980, A&A 87, L1

Mukai K., 1990, PASP 102, 183

Palla F., Stahler S.W., 1993, ApJ 418, 414

Pasquini L., Cutispoto G., Gratton R., Mayor M., 1991, A&A 248, 72

Petrov P.P., Gullbring E., Ilyin I., et al., 1996, A&A 314, 821

Piskunov N.E., Tuominen I., Vilhu O., 1990, A&A 230, 363

Praderie F., Simon T., Catala C., Boesgaard A.M., 1986, ApJ 303, 311

Press W.H., Teukolsky S.A., Vetterling W.T., Flannery B.P., 1992, Numerical Recipes, Second Edition. Cambridge University Press, Cambridge

Robinson R.D., 1980, ApJ 239, 961

Rüedi I., Solanki S.K., Mathys G., Saar S.H., 1997, A&A 318, 429

Saar S.H., Solanki S.K., 1992, in: Giampapa M.S., Bookbinder J.A. (eds.), 7th Cambridge Workshop on "Cool Stars, Stellar Systems and the Sun". PASP Conf. Series 26, p. 259

Saar S.H., Piskunov N.E., Tuominen I., 1992, in: Giampapa M.S., Bookbinder J.A. (eds.), 7th Cambridge Workshop on "Cool Stars, Stellar Systems and the Sun". PASP Conf. Series 26, p. 255

Saar S.H., Piskunov N.E., Tuominen I., 1994, in: Caillault J.-P. (eds.), 8th Cambridge Workshop on "Cool Stars, Stellar Systems and the Sun". PASP Conf. Series 64, p. 661

Schaller G., Schaerer D., Meynet G., Maeder A., 1992, A&AS 96, 269

Schrijver C.J., 1993, A&A 269, 446

Semel M., 1987, A&A 178, 257

Semel M., 1989, A&A 225, 456

Semel M., Donati J.-F., Rees D.E., 1993, A&A 278, 231

Semel M., Li J., 1995, Solar Phys. 164, 417

Simon T., Landsman W., 1991, ApJ 380, 200

Strassmeier K.G., 1990, A&A 348, 682

Strassmeier K.G., Welty A.D., Rice J.B., 1994, A&A 285, L17

Strassmeier K.G., Hall D.S., Fekel F.C., Scheck M., 1993a, A&AS 100, 173

Strassmeier K.G., Rice J.B., Wehlau W.H., Hill G.M., Matthews J.M., 1993b, A&A 268, 671

Thompson I.B., Landstreet J.D., 1985, ApJ 289, L9

Tinbergen J., Rutten R., 1992, WHT User Manual # 21

Valenti J.A., Marcy G.W., Basri G., 1995, ApJ 439, 939

Vigneron C., Mangeney A., Catala C., Schatzman E., 1990, Solar Phys. 128, 287

Vilhu O., Gustafsson B., Walter F.M., 1991, A&A 241, 167

Vogt S.S., 1981, ApJ 247, 975

Vogt S.S., Hatzes A.P., Misch A.A., Kürster M., 1997, ApJS (submitted)

Zahn J.-P., Bouchet L., 1989, A&A 223, 112